



IMPACT OF FRACTURES ON FLUID FLOW DURING WATERFLOODING IN CARBONATE ROCKS

JHON ALEXANDER BARRERA MARIN

Master Thesis
Master's degree in petroleum engineering
March 2020

Supervisors:

Nikolai Andrianov

Hamid Nick

Vera Rocca

Politecnico di Torino
Danish Hydrocarbon Research and Technology Center
Technical University of Denmark

Abstract

Improving oil recovery in carbonate reservoirs is one of the main subject areas for research and technology development. As most of carbonate reservoirs are naturally fractured [1], oil recovery is considered to be a great challenge because of the complex fracture-matrix interactions and heterogeneous properties of the reservoir. In this thesis, waterflood efficiency in fractured carbonate reservoirs is studied by using a two-dimensional Discrete Fracture-Matrix (DFM) model, which is based on a representative outcrop of the North Sea reservoirs.

In the first part of the thesis, we set up the DFM model for fluid flow in porous media, in order to investigate how different mechanisms influence the recovery of hydrocarbons. The flooding simulations are performed by injecting sea water and diluted sea water, and three different scenarios of variable fracture aperture are considered in distinct sector models of the outcrop. Simulations show that apertures and orientation of the fractures, in combination with the fracture-matrix permeability ratio can considerably affect the oil recovery efficiency. In addition, we analyze the effect of a far-field applied stress on the fluid flow behavior by changing the orientation of the maximum applied stress on the fractured model.

Besides, we consider adsorption processes between the injected water and the carbonate rock, which researchers believe to be one of the key phenomena behind low salinity water (LSW) flooding effect [2]. Adsorption parameters are evaluated and compared to determine any low salinity effect of the diluted sea water injected on oil recovery. We show that a retardation in the water saturation front is observed as a result of the adsorption processes.

Table of Contents

Abstract	2
List of Figures	5
List of Tables	7
Nomenclature	8
INTRODUCTION	9
2. METODOLOGY.....	13
2.1 Geological Setting.....	13
2.2 Fracture Aperture Distribution model.....	15
Barton-Bandis Model	15
2.2 Numerical Method	19
Discrete Fracture Network Model.....	19
2.3 Production from fractured carbonated reservoirs.....	20
2.4 Transport Model in Fractured Porous Media.....	20
Governing Equations	21
Adsorption Model	24
3. SIMULATION RESULTS.....	26
3.1 Waterflooding Simulations Scenarios	26
3.2 Sea Water Flooding Simulation	28
3.2.1 Uniform Aperture Distribution.....	28
Fracture Pattern Effect on Fluid Flow Behavior	28
Injection Rate Effect on Oil Recovery	30
Fracture Aperture effect on Oil Recovery.....	30
3.2.2 Variable Aperture Barton-Bandis distribution	32

Orientation Stress Effect on Oil Recovery.....	34
3.2.3 Comparison between Uniform vs. Variable fracture aperture	36
Matrix Permeability Effect on Fluid Flow	38
3.3 LSW Simulations.....	40
Fractured and No Fractured Model Comparison	40
Effect of Water Injection Rate on Oil Recovery.....	41
SW flooding and LSW Flooding Comparison	42
3.4 LSW Simulations considering Adsorption Processes.....	43
Sensitivity Analysis of Adsorption Parameters	45
CONCLUSIONS.....	47
References	49

List of Figures

Figure 1. Schematic block diagram of the tectonic situation of the quarries on salt ridge Krempe ..	13
Figure 2. (a) Fracture trace map, and (b) Estimated fracture density map for the Lägerdorf profile section	14
Figure 3. (a) Fracture traces map and (b) Rose diagrams of fractures distribution orientation of the three selected section models.....	15
Figure 4. Empirical hyperbolic function between normal stress and fracture closure.....	16
Figure 5. Fracture cross section model of the induced opening. A far-field maximum (σ_1) and minimum (σ_3) principal stresses induce a normal stress (σ_n)on the fracture walls.....	17
Figure 6. Schematic representation of the hydraulic and mechanical aperture	18
Figure 7. Discretize highly fracture network sector. The blue lines indicate fractures and the green lines represent the triangulated matrix discretization	19
Figure 8. Relative permeabilities and capillary pressure curve for pure SW (blue lines) and LSW (red lines).	23
Figure 9. Schematic representation of the boundaries condition in the model	27
Figure 10. Snapshots of oil saturation front after 60 days of waterflooding using an injection rate of 1e-6 [m ³ /s] and fracture aperture of 1e-5 [m].....	27
Figure 11. Recovery factor versus time (days) and Pore Volume (PV) of injected water using three different fracture sector model.	29
Figure 12. Snapshot of the fluid behavior in different fracture pattern models after 10 days of waterflooding.....	29
Figure 13. Recovery factor and WCT for waterflooding in the highly fractured model for a uniform aperture of 1x10-4[m].....	30
Figure 14. Recovery factor and WCT for waterflooding in the highly fractured model for uniform aperture of 1x10-4 [m], 5x10-4 [m] and 1x10-3 [m].	31
Figure 15. Snapshot of the fluid behavior in the highly fractured pattern model after 100 days of waterflooding.....	31
Figure 16. Fracture and frequency aperture distribution according to the orientation of the maximum stress applied in the fractured sector models.....	33

Figure 17. Oil recovery and WCT plot as a function of time for the anisotropic sector model, with injection rate of $1 \times 10^{-5} [\text{m}^3/\text{s}]$. applied in x and y direction.	34
Figure 18. Snapshots of the anisotropic sector model in the x-direction (top) and y-direction (bottom) using injection rate of $1 \times 10^{-5} [\text{m}^3/\text{s}]$ after 4 days of waterflooding.	35
Figure 19. Oil recovery and WCT plot as a function of time for the highly fractured sector model, with injection rate of $1 \times 10^{-5} [\text{m}^3/\text{s}]$. applied in the constant aperture model and in the two Barton-Bandis scenarios ($\alpha = 0^\circ$ and $\alpha = 90^\circ$).	37
Figure 20. Snapshots of the highly fractured sector model using an injection rate of $1 \times 10^{-5} [\text{m}^3/\text{s}]$ for the constant aperture model and the two Barton-Bandis scenarios ($\alpha = 0^\circ$ and $\alpha = 90^\circ$). after 20 days (top) and 40 days (bottom) of waterflooding.	37
Figure 21. Oil recovery and WCT plot as a function of time for the highly fractured sector model, with injection rate of $1 \times 10^{-5} [\text{m}^3/\text{s}]$. for the Barton-Bandis scenarios when ($\alpha = 0^\circ$)	39
Figure 22. . Snapshots of the highly fractured sector model using an injection rate of $1 \times 10^{-5} [\text{m}^3/\text{s}]$. (a) for waterflooding simulations with high matrix/permeability contrast and (b) for the case of waterflooding simulations with low matrix/permeability contrast.....	39
Figure 23. Recovery factors and WCT vs time for LSW flooding in a highly fractured model (black lines) and a model without fractures (red lines).	40
Figure 24. Snapshots of LSW flooding after 500 days for a highly fractured model (a) and a model without fractures.	41
Figure 25. Recovery factors and WCT vs time for LSW flooding in a highly fractured under different injection flow rates.....	42
Figure 26. Recovery factors and WCT vs time for SW and LSW flooding in highly fractured model... ..	42
Figure 27. Recovery factors and WCT vs time for two set of simulation the adsorption and No adsorption model in the highly fractured sector model.	43
Figure 28. Snapshots of LSW flooding for two set of simulation the adsorption and No adsorption model in the highly fractured sector model after 170 and 470 days.	44
Figure 29. Recovery factors vs time for the sensitivity the adsorption model in the highly fractured sector model.	46

List of Tables

Table 1. Oil-water relative permeabilities used in simulations	23
Table 2. Rock and fluid properties	26
Table 3. Average aperture and fracture permeability in the fractured sector models by applying Barton-Bandis model when maximum principal stress σ_1 is applied at $\alpha = 0^\circ$ and $\alpha = 90^\circ$	32
Table 4. Fracture permeabilities and fracture-matrix permeability ratio for different scenarios.....	38
Table 5. Fracture permeabilities and fracture-matrix permeability ratio for different scenarios.....	36
Table 6. Summary of the sensitivity cases and adsorption parameters values.....	43

Nomenclature

Δu	=	Fracture closure	[m]
σ_n	=	Normal stress acting on fracture plane	[MPa]
σ_1	=	Maximum principal stress	[MPa]
σ_2	=	Minimum principal stress	[MPa]
E_0	=	Initial unstressed aperture	[m]
E_n	=	Mechanical aperture at normal stress	[m]
e	=	Hydraulic fracture	[m]
k_f	=	Fracture Permeability	[m ²]
S	=	Fluid saturation	[-]
u	=	Darcy velocity	[m ³ /s]
ϕ	=	Porosity	[-]
μ	=	Fluid Viscosity	[cP]
ρ	=	Fluid density	[kg/m ³]
P	=	Fluid pressure	[Pa]
g	=	Gravity acceleration	[m/s ²]
f_w	=	Fractional flow	[-]
x	=	Molar fraction	[-]
X	=	Mass fraction	[-]
ξ	=	Molar density	

Abbreviations

SW	=	Sea Water
LSW	=	Low Salinity Water
EOR	=	Enhanced Oil Recovery
DFM	=	Discrete Fracture-Matrix
JRC	=	Joint Roughness Coefficient
WCT	=	Water Cut
PV	=	Pore Volume

INTRODUCTION

Waterflooding is one of the most common methods used for hydrocarbon recovery, once the production under primary drive mechanisms such as water drive, expansion drive, or compaction drive are insufficient [3]. Although, it has been broadly applied in light crude oil reservoirs, waterflooding in high viscosity heavy oil reservoirs is often employed at early production time [4]. Even though waterflooding has been implemented for decades, technical limitations and constraints including corrosion in production pipes, high water production rates, and compatibility between injected water and the reservoir connate water, have avoided unlocking its real potential [5]. For this reason, during the past few years, a series of advances have been developed in order to reduce limitations and improve waterflooding processes. From these advances, Low Salinity Waterflooding (LSW) has emerged as a new Enhanced Oil Recovery (EOR) technique, which is designed to inject water with different chemical properties instead of any available water that has been injected or planned to inject [2]. EOR is the implementation of different techniques for incrementing the volume of oil that can be recovered from a reservoir [6], which are aimed at changing the physical and chemical properties of the rock [7]. Diverse EOR strategies may be selected based on reservoir fluid, rock characteristics and the current production stages [8].

The first ones to develop the concept of reducing the salinity of water to improve the displacement of fluids in waterflood projects were Tang and Morrow [9], who performed different experimental tests in sandstone formations. Later on, Yousef et al. [2] carried out several experiments in core samples from carbonates formations. Some of these experiments showed positive effects of LSW on improving oil recovery. Since then, the main area of research has been to understand the complex chemical reactions between oil, water and rock [6], which could explain the mechanism by which LSW may perform better than traditional methods using high salinity waterflooding [10].

Although most of the research related to LSW has been centered on sandstone reservoirs, LSW in carbonate formations has gained considerable acceptance as potential prospects [11]. This is due to

the presence of large carbonate oil reservoirs in North Sea and Middle East, which require efficient and economically attractive methods for enhancing recovery [12, 13].

There is no consensual explanation on the effect of the salinity reduction of the injected water on the oil recovery in carbonate reservoirs. However, due to the increase of experimental data and field evidence, a number of mechanisms have been proposed to describe this phenomenon [14, 11]. Some of the relevant studies in the literature are focused on: changes in wettability of carbonate surfaces from less to more water-wet condition due to rock dissolution [13], double layer expansion [15], or surface charge modification [16]. Similarly, permeability changes and interfacial tension reduction have been proposed to evaluate the benefit of lowering water salinity on oil recovery [17].

Hiorth et al. [15] suggests that when water is injected into a reservoir, the thermodynamic equilibrium between water, oil and rock is interrupted. Some minerals dissolve in injected water to restore the equilibrium, and this may change the wettability, producing an additional oil recovery. The hypothesis behind this phenomenon could be physically explained by Multicomponent Ion Exchange (MIE) theory proposed by Lager et al. [18]. The MIE process leads to the adsorption of divalent ions and promotes the mineral dissolution/precipitation. Moreover, this process can change the ionic composition of formation water and the wettability condition [19].

Production enhancement by LSW in fractured carbonate formations represents a challenge. Fractured carbonate reservoirs can present highly varying properties (i.e., porosity, permeability, fracture aperture) within small sections of the reservoir. Understanding the impact of fractures and the complex interaction at different interfaces (i.e., oil-rock, oil-water, and water-rock) on the flow properties are fundamental for the behavior prediction of this type of rock [11]. In addition, such reservoirs present a matrix/fracture flow exchange as one of the main mechanisms of production [20], which make them arduous to characterize.

Several researchers have shown ideal results in the representation of this complex fracture media by using Discrete Fracture-Matrix (DFM) models. DFM models consider the contribution on the fluid flow of individual fractures, fracture networks and the matrix at the same moment [21]. Additionally, the

model can describe the fractures as lower-dimensional entities into the domain, which allows reducing the mesh by diminishing of the total amount of discretized elements [22]. However, in order to adequately reproduce flow behavior in the reservoir, reliable data of the fracture network and rock properties are required.

By means of the study of outcrops, it is possible to directly investigate the geological characteristics of a reservoir, obtaining important information regarding the size, orientation, location and aperture of the fracture network [23]. Analysis of the analog outcrops is a useful tool that allow digitalizing fractures and obtaining a more realistic representation of the fracture network. As a result, reliable flow simulation models could be generated producing a better description of the flow behavior in the reservoir [24].

The objective of this work is to evaluate, firstly, different scenarios related to water injection processes in naturally fractured carbonate reservoirs in the North Sea. We try to find more precise answer on the following questions: Is the oil recovery affected by the aperture fracture distribution according to the orientation of the far-field stress in the domain? If the aperture distribution is considered as uniform, what would be the impact of the assumption, compared with an aperture distribution based on the Barton-Bandis approach? Secondly, we try to examine how adsorption process affects the hydrocarbon recovery under changes in injection rates, fracture apertures and homogeneity of the system, as well as evaluate the impact of the adsorption parameters on the performance of LSW flooding processes.

In order to study the waterflood performance in carbonate reservoirs, a DFM model is created using the dataset obtained from direct observation and photographs of the walls of an outcrop representative of North Sea fracture chalk reservoirs, which is exposed at Lægerdorf, northwest Germany [25]. In this model, the traces of the fractures are represented as one-dimensional faces embedded in a two-dimensional matrix domain, and the fluid and rock properties used are from characteristic reservoirs of the North Sea. We use DuMuX, a free and open-source simulator for flow and transport processes in porous media where the numerical model developed by Gläser et al. is

implemented [22], in order to simulate waterflooding processes and analyze how oil recovery is affected by changes in fracture aperture distribution and injection rate.

The study is organized as follows: First, the geological characteristics of a representative outcrop are showed, followed by the selection of the sector models used in simulations. Second, the aperture distribution model is presented. Third, the governing equations used in the different flow fluid models are explained. And fourth, we present the simulation results of the selected waterflood scenarios. The results highlight the impact of fracture network, fracture aperture and fracture-matrix permeability ratio on oil recovery. Orientation of the applied principal stress plays an important role on the fracture aperture distribution which can vary flow behavior in the fractured model. We simulate LSW flooding with and without considering adsorption processes and examine how the oil recovery is influenced by changes in adsorption parameters.

2. METODOLOGY

2.1 Geological Setting

The Upper Cretaceous Chalk, which is exposed in Lägerdorf area (**Figure 1**) in northwest Germany, is an outcrop analogue for hydrocarbon reservoirs in the North Sea fractured chalk reservoirs, because it was deposited in the same basin setting by the same depositional system as the offshore reservoirs [26].

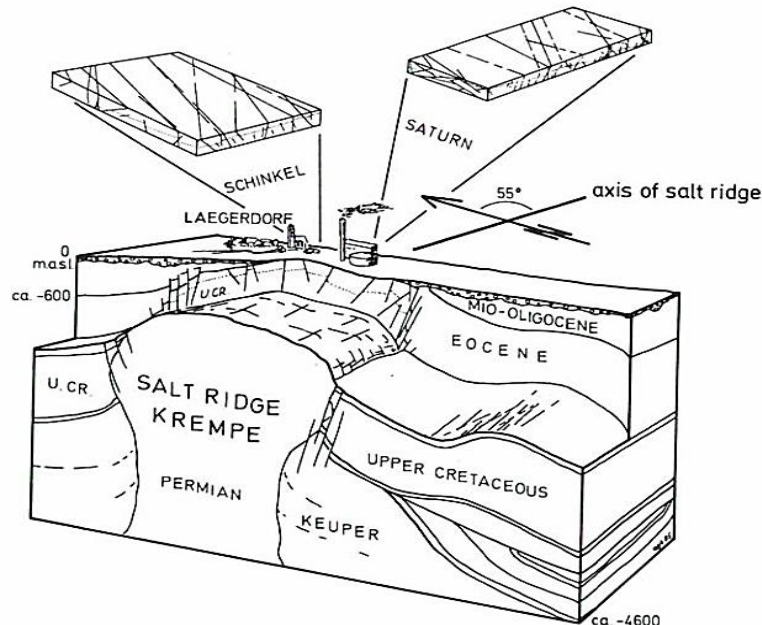


Figure 1. Schematic block diagram of the tectonic situation of the quarries on salt ridge Krempe [27].

These Upper Cretaceous chalks are exposed at the surface due to the rise of the underlying Krempe salt ridge, where the exploited quarries of Lägerdorf provide an excellent exposure of the chalks by more than 1000 m long, 60 m deep and several hundred meters wide [27]. Different deformation features are present in the formation because of superimposed stresses, which are concentrated on distinct faults zones with different complex structures [28].

The outcrop area provides a wider and more detailed view of fracture type and heterogeneity in the reservoir as compared to limited subsurface data. The geological features in the production wall of

the quarry were characterized and mapped at different scales by Koestler and Ehrmann [25]. From this characterization, a 250 m long and 50 m wide profile section (**Figure 2a**) in the wall of the quarry was studied in terms of fracture distribution, orientation and length [26]. This formation exposure can help in decreasing reservoir description uncertainty by improving the understanding of those geological parameters that can affect the flow behavior through the reservoir [29].

Using FracPaQ [30], a Matlab toolbox for the quantification of fracture patterns, the fracture density map was estimated for the profile section of the quarry . The estimated fracture intensity map (**Figure 2b**) shows three or more discrete groups of high density (i.e. a high number of fractures per square metre). Three sectors of high fracture density in the profile section were selected in order to analyze the effects of fractures on oil recovery during simulations. The sectors are distinctly characterized as follows:

- ✓ **Highly fractured section:** high fracture density and variable fracture orientation.
- ✓ **Anisotropic section:** mostly vertical fracture orientation.
- ✓ **Isolated section:** isolated fractures.

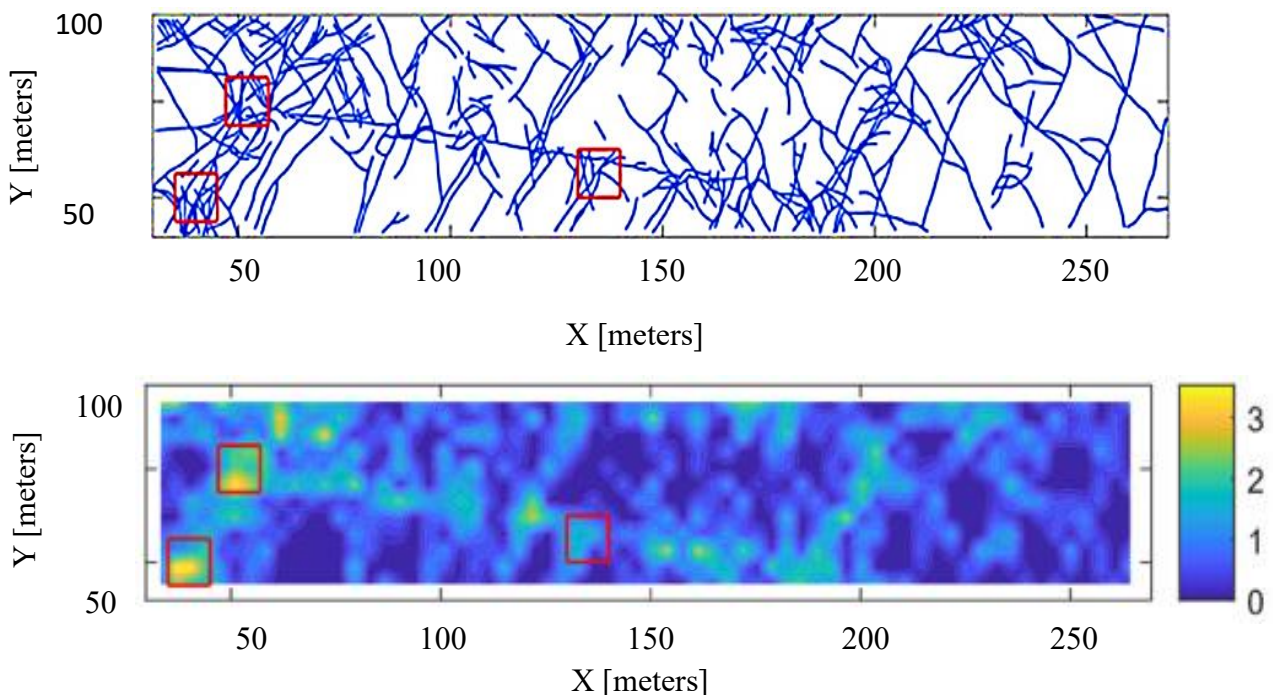


Figure 2. (a) Fracture trace map, and (b) Estimated fracture density map for the Lägerdorf profile section [31].

Figure 3 shows the fracture traces map and the distribution of fractures angles of the three different sectors. Highly fractured sector shows a more homogeneous distribution of fracture angles compared with the anisotropic sector, which is more vertically orientated.

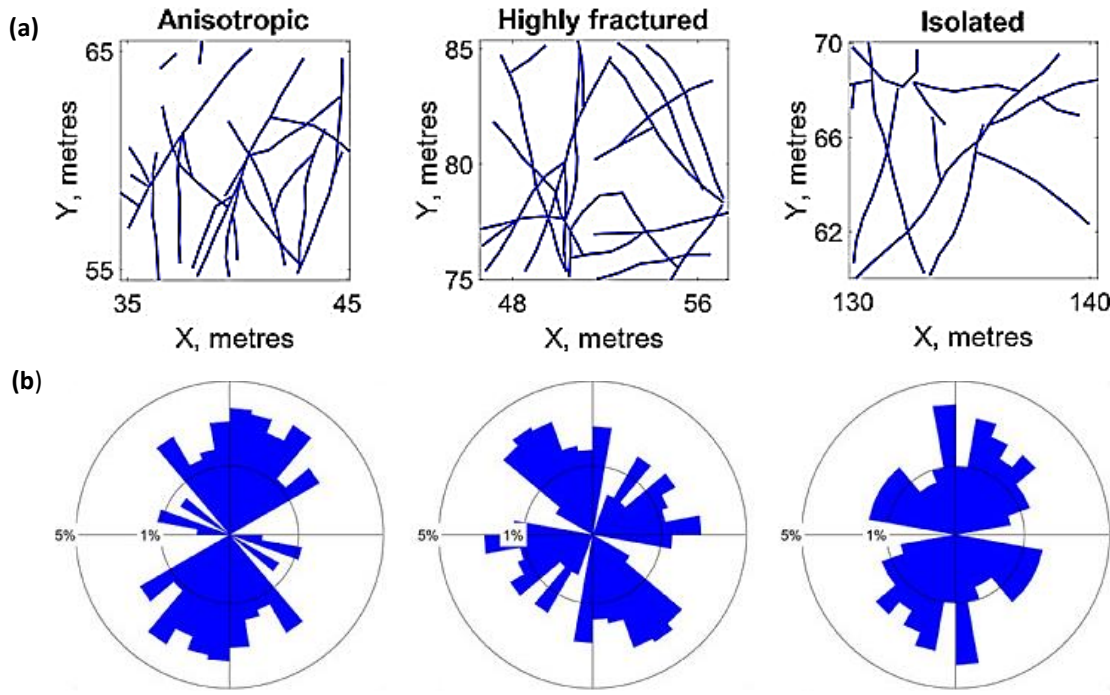


Figure 3. (a) Fracture traces map and (b) Rose diagrams of fractures distribution orientation of the three selected section models [31].

2.2 Fracture Aperture Distribution model

Barton-Bandis Model

Natural fractures in a porous medium are planar and non-planar discontinuities in rocks [32], which are present as local breaks and have different characteristics than the medium itself. These fractures are formed due to the combined effect of the mechanical properties of the rock and historical deformations events that the rock have experienced, such as tectonic movement, lithostatic pressure changes, high fluid pressure, etc. [33]. These deformation events govern certain fracture properties, such as aperture, connectivity and distribution. For instance, an efficient characterization of fractures will allow to reduce uncertainties in the model [34]. Several researches

have proposed reducing uncertainty by using different approaches to maintain the geological consistency [35].

One of the approaches is the Barton-Bandis model, which allows to determine the aperture of a fracture using the mechanical properties of the rock [36]. This fracture aperture is considered as the separation between the opposing walls of a fracture, and plays an important role with respect to the fracture conductivity and can be comparable to pore geometry of the rock matrix [37].

Bandis et al. [38] and Barton et al. [39] described the effects of surface roughness on discontinuity deformation and strength as a function of an empirical relation between stress and deformation components. The following expression shows a hyperbolic empirical relationship between the normal stresses (σ_n) and the fracture closure ($\Delta\nu$), which corresponds to the aperture fracture reduction due to normal closure:

$$\Delta\nu = \frac{a \sigma_n}{(1 + b \sigma_n)} , \quad (1)$$

where a and b are constants.

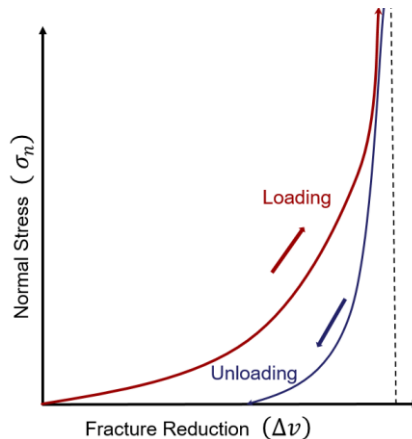


Figure 4. Empirical hyperbolic function between normal stress and fracture closure [38].

A stress-dependent aperture variable E_n is defined by Bandis et al. [38] as a function of a hyperbolic relationship (1):

$$E_n = E_0 - \frac{a \sigma_n}{(1 + b \sigma_n)} , \quad (2)$$

where E_0 is the initial unstressed aperture. The normal stress acting on each fracture segment is calculated using Cauchy's equation:

$$\sigma_n = \sigma_1 \sin^2 \theta - \sigma_3 \cos^2 \theta , \quad (3)$$

in which σ_1 and σ_3 represent the maximum and minimum compressive principal stresses acting in the plane of the matrix rock, respectively; and θ is the angle between σ_1 and σ_n (**Figure 5**).

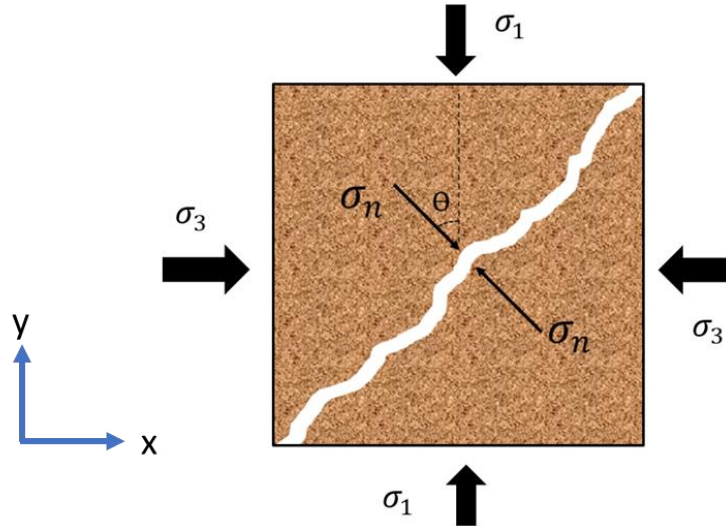


Figure 5. Fracture cross section model of the induced opening. A far-field maximum (σ_1) and minimum (σ_3) principal stresses induce a normal stress (σ_n) on the fracture walls [40].

Initially, all the fractures have an initial mechanical aperture under no stress condition. Apertures are determined using Barton-Bandis model by assuming a scenario representative for Central North Sea [41] with a shallow burial depth of 1300 m with principal stresses $\sigma_1 = 26.7$ MPa and $\sigma_3 = 10$ MPa. The applied stress conditions used in the model result from the application of Terzaghi's law for geostatic stresses, considering that the stresses induced by pore fluid and rock matrix only includes normal stress [42]. These considered stresses values are based on an Upper Cretaceous-Danian chalk reservoir described on Japsen et al [43].

The fluid flow in the fracture is approximately described as classical Darcy flow, and the permeability calculation is based on the cubic law [44]. This law assumes that a fracture is represented by two smooth parallel plates separated by an equivalent hydraulic aperture e , hence the intrinsic fracture permeability (k_f) can be calculated as follows [45]:

$$k_f = \frac{e^2}{12} , \quad (4)$$

Following the cubic law, Barton et al. [46] propose an empirical equation to convert values of mechanical values (E) into hydraulic aperture values (e) by means of the following equation:

$$e = \frac{E^2}{JRC^{2.5}} , \quad (5)$$

where the Joint Roughness Coefficient (JRC) is a dimensionless value estimated by roughness profile matching or measured using the fracture amplitude-length ratio. **Figure 6** shows a visual representation of the fracture cross-section in the Barton-Bandis model.

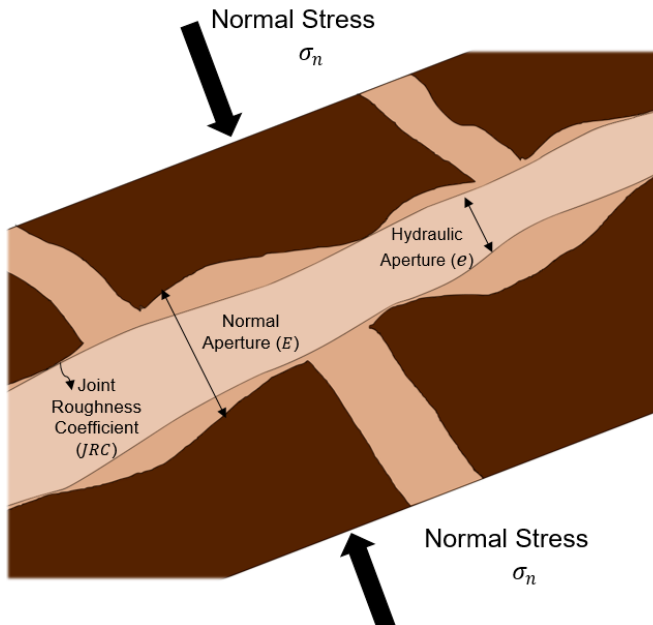


Figure 6. Schematic representation of the hydraulic and mechanical aperture [47].

2.2 Numerical Method

Understanding of the effects of fractures on fluid flow behavior through the reservoir is fundamental to evaluate efficiency in a waterflood process, because of the fact that fractures can dramatically affect local permeability and thereby enhance production rates [48]. Numerical reservoir simulation is applied in order to forecast the fluid flow behavior in hydrocarbon reservoirs [49]. In the case of fractured carbonates reservoirs, one of the most important aspect of modeling is the accurate calculation of fluid exchange between the matrix and the fractures [50]. Moreover, modelling of fractured carbonate reservoirs with complex fractures networks requires adequate representations of individual fractures and fractures networks, with different size, orientation, spatial distribution, fracture density and aperture [23].

Discrete Fracture Network Model

A Discrete Fracture-Matrix (DFM) model is used to represent three $10 \text{ [m]} \times 10 \text{ [m]}$ sectors of the mapped outcrop area previously selected [31]. DFM models explicitly consider the fluid flow contribution of individual fractures, fracture networks and matrix in the model structure [23]

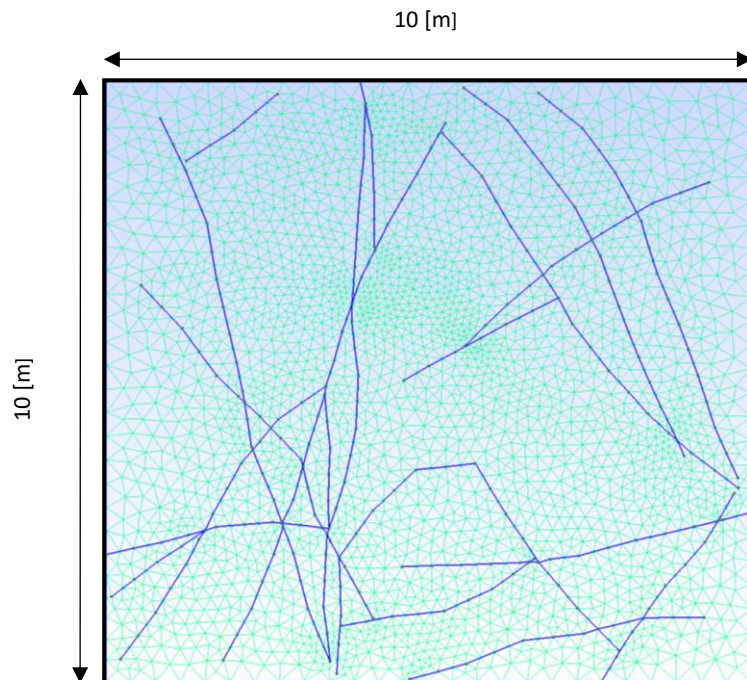


Figure 7. Discretize highly fracture network sector. The blue lines indicate fractures and the green lines represent the triangulated matrix discretization [31].

The rock matrix from the mapped outcrop is discretized by 2D triangulated elements and the fractures are specifically represented as low dimensional entities in the domain [51]. **Figure 7** shows the discretization of the highly fractured sector model, which can be characterized with a relatively isotropic fracture orientation distribution and with 472 fracture segments [31].

2.3 Production from fractured carbonated reservoirs

Fractured reservoirs may result from stresses exceeding the rock strength [52]. Carbonate reservoirs are characterized by heterogenous rock properties and complex fractured network systems [53]. This geological structures in the rock influence flow behavior during production. Planning the production from carbonate reservoirs require precise and consolidate geological description of the reservoir. The main oil production mechanism in fractured carbonate rocks is gravity drainage, which control oil production by considering interactions between the upper and lower blocks [54]. In these reservoirs, flow is predominantly conducted through fracture networks, and fracture permeability generally determines the performance of the produced wells [55].

2.4 Transport Model in Fractured Porous Media

The presence of natural fractures can affect the transport of fluids in porous media. Therefore, it is a great challenge to develop a model that accurately represents the impact of fractures on waterflood performance [23]. Additionally, during Low Salinity waterflooding, adsorption processes may occur due to geochemical flow interaction between the injected water and the porous media. To model the effect of adsorption reactions is required a proper interpretation of a fundamental concept called adsorption isotherms. The overall understanding of this concept allows an effective design of the adsorption model [56]. The model considered in this study is a two-phase flow model based on the conservation of mass, constitutive equations and equations of state, where the fluids are immiscible and there is not mass transfer between the phases in porous media [57].

Governing Equations

In this section, we present the governing equations for multiphase flow. Firstly, in order to deal with multiphase flow, we introduce the notion of saturation S_α and porosity φ . Porosity is considered as the volume of void space available for fluids expressed in volumetric fraction, and saturation (S_α) as the fraction of the pore space filled by phase α , which in this study are oil and water [57]. From this definition, saturations satisfy the following relationship,

$$\sum_\alpha S_\alpha = 1. \quad (6)$$

Following the generalized Darcy's model, the superficial velocity of each phase α can be calculated as,

$$u_\alpha = -\frac{\mathbf{K}_\alpha}{\mu_\alpha} \nabla (P_\alpha - \rho_\alpha g Z) \quad \alpha = w, o , \quad (7)$$

where the subscript “ w ” represents the water phase and subscript “ o ” represents the oil phase, and the apparent permeability \mathbf{K}_α is given by:

$$\mathbf{K}_\alpha = \mathbf{K} k_{r\alpha}(S_\alpha). \quad (8)$$

Here \mathbf{K} is the permeability tensor of the porous medium, $k_{r\alpha}(S_\alpha)$ is the relative permeability of the phase α , μ_α is the viscosity of phase α , P_α stands for the pressure of the phase α , the mass density of phase α is denoted by ρ_α , and the gravity acceleration with \mathbf{g} . It is important to notice that when water is injected, it flows around sections of porous media occupied by oil, which means that the space available for one of the fluids depends on the amount of the other fluid filling the pore space [58], but also by additional interaction between the fluids. The pressure difference (P_{cow}) between a wetting (P_w) and a non-wetting (P_n) phases are calculated according to the following relationship,

$$P_{cow} = P_n - P_w . \quad (9)$$

For the purposes of waterflood modeling, when a phase α consists of multiple components k , which can either be a pure chemical substance or consist of different substances, the mass conservation holds for each component. Therefore, the mass conservation equation is written as:

$$\varphi \frac{\partial [\sum_{\alpha} x_{\alpha}^k \xi_{\alpha} s_{\alpha}]}{\partial t} + \nabla \cdot (\sum_{\alpha} x_{\alpha}^k \xi_{\alpha} u_{\alpha}) = 0 \quad \alpha = w, o \quad k = S, L, O \quad , \quad (10)$$

where the superscript $k = S, L, O$ indicate respectively a *SW*, *LSW* and oil component. Here x_{α}^k is the mole fractions used for each component k in phase α , and ξ_{α} is the molar density of phase α .

The model is developed supposing that the *SW*, *LSW* and oil components are under conditions of thermodynamic equilibrium, which means that there is not spontaneous changes in the macroscopic properties of the system [59]. The multicomponent systems are in thermodynamic equilibrium when Gibbs free energy is a minimum at constant pressure (P), temperature (T):

$$f_w^k(T, P_w, x_w^k) = f_o^k(T, P_o, x_o^k)$$

where f_w^k and f_o^k are the fugacity functions components k in phase α .

To study the effect of the injection of low-salinity water, the model was built assuming identical properties for sea water (SW) brine and low-salinity water (LSW) brine such as density and viscosity but using different relative permeability and capillary pressure curves. In this model, it is assumed that where SW is blended with LSW, water/oil relative permeabilities and capillary pressure are interpolated between the values corresponding to pure SW and pure LSW. By using the Brooks-Corey model [60], the relative permeabilities for pure SW and pure LSW are calculated for a given saturation between the end points,

$$k_{rw}^k = k_w^k (S_{we}^k)^{n_w^k} \quad k = S, L \quad , \quad (11)$$

where the subscripts S and L refer to SW and LSW, k_w^k and k_o^k are the water and oil end point relative permeabilities, n_w^k and n_o^k are Corey's exponent for water and oil respectively, and S_{we}^k denotes the effective water saturations, which can be obtained by the following equation:

$$S_{we}^k = \frac{S_w - S_{wr}^k}{1 - S_{wr}^k - S_{or}^k} \quad . \quad (12)$$

Here, S_{wr}^k and S_{or}^k are residual water and oil saturations, respectively.

In order to obtain the water/oil relative permeabilities values when water is a mixture of SW and LSW, we use the following linear interpolation model:

$$k_{rw} = x_w^S k_{rw}^S + (1 - x_w^S)k_{rw}^L \quad k_{ro} = x_w^S k_{ro}^S + (1 - x_w^S)k_{ro}^L \quad (13)$$

where x_w^S denote the molar fraction of SW in water phase.

The above methodology is described in Chen et al. [61] and Helmig et al. [57], as a representative correlation during the LSW flooding which is employed in this simulation. **Figure 8** shows the relative permeability and capillary pressure curves for pure SW and pure LSW condition, which were extracted from a research conducted by Graue et al. [62]. Graue et al. performed different waterflooding experiments in larger blocks of fractured chalk using North Sea crude oil. The SW and LSW relative permeability parameters used for the model are shown in the following table.

Waterflooding phase	k_w	k_o	n_w	n_o	S_{wr}	S_{or}
1 st Pure SW	0.394	0.202	2.053	2.016	0.103	0.355
2 nd Pure LSW	0.262	0.976	3.999	1.210	0.103	0.132

Table 1. The parameters of oil-water relative permeabilities used in simulations

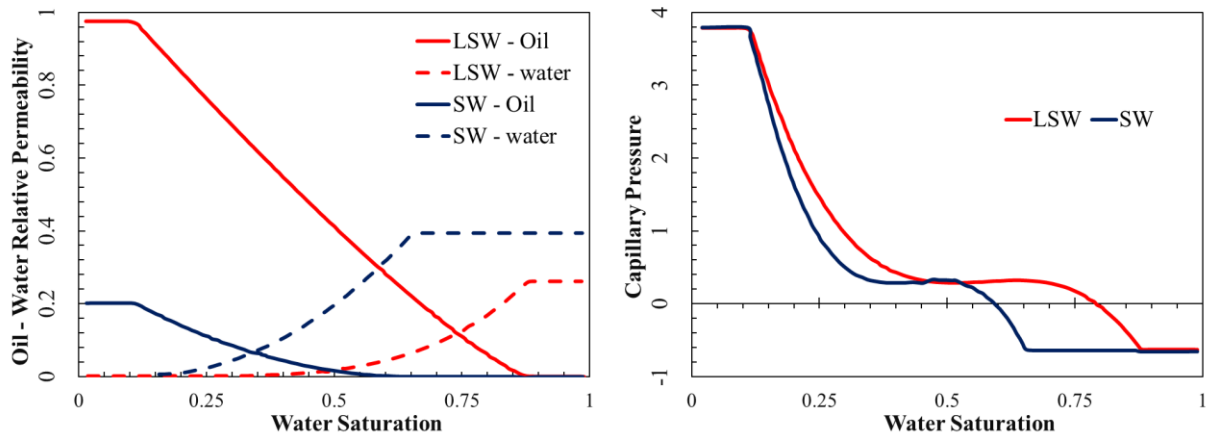


Figure 8. Relative permeabilities and capillary pressure curve for pure SW (blue lines) and LSW (red lines).

In **Figure 8(left)**, the initial state of the reservoir shows an oil-wet behavior and after the low salinity waterflooding a more water-wet behavior. Also, it can be observed in **Figure 8(right)**, LSW imbibition capillary pressure curve is located above SW curve, which evidences that the spontaneous imbibition in LSW condition is more predominant than in SW condition.

Adsorption Model

The impact of LSW is generally related to the change of the wetting phase of the rock [63]. Therefore, it is necessary to relate wetting state to the geochemical processes on the rock surface. This can be reached by considering the adsorption process occurs between the rock phase and the *LSW* component in water phase.

To evaluate the effect of adsorption on the performance of a waterflooding process in a porous media. A model for the two-phase flow in porous media is introduced in **Equation 14** by applying the concept of fractional flow, molar fraction and molar concentration. We derive the mass conservation equation expressed as follows [57] [61],

$$\frac{\partial}{\partial t} [\varphi X_w^L \rho_w S_w + (1 - \varphi) X_R^L \rho_R] + \nabla \cdot (X_w^L \xi_w f_w u_t) = 0 \quad (14)$$

where the subscript “R” represents the rock phase, f_w is the fractional flow, X_R^L is the mass fraction of the *LSW* component in water phase, and u_t is the total velocity. From this equation, a retardation term is defined in **Equation 15**. This retardation coefficient relates the retardation effect of the LWS front which is caused by the adsorption process.

$$\text{Retardation} = (1 - \varphi) X_R^L \rho_R \quad (15)$$

When LSW is injected, a front of different concentration travel through the porous space in the direction of the fluid flow. **Equation 15** shows that the chemical solute concentration travels slow than the solution (water), which is caused by the adsorption of ions on the porous rock.

The adsorption can be defined using adsorption isotherm models, which correlate the concentration equilibrium between the solute in the solution and the adsorbent rock [64]. In this model, three adsorption isotherm relationship are considered. By assuming that the density of water and rock are maintained constant, we can state the following relationship $X_w^L \rho_w = x_w^L \xi_w M^L$. The following equilibrium relationship have been used in the model:

- **Linear Isotherm:** $X_R^L = \gamma X_w^L = \gamma x_w^L \xi_w M^L = \tilde{\gamma} x_w^L$.

- **Freundlich Isotherm:** $X_R^L = \gamma (X_w^L)^n = \gamma (x_w^L)^n \xi_w M^L = \tilde{\gamma} (x_w^L)^n$.

- **Langmuir Isotherm:**

$$X_R^L = \frac{\gamma_1 (X_w^L)^n}{1 + \gamma_2 X_w^L} = \frac{\gamma_1 (x_w^L)^n \xi_w M^L}{1 + \gamma_2 x_w^L \xi_w M^L} = \frac{\tilde{\gamma}_1 (x_w^L)^n}{1 + \tilde{\gamma}_2 x_w^L}$$

where γ , $\tilde{\gamma}$ and n are empirical constants which depend on the absorption properties of the rock surface, and the properties of the injected water. Both can be obtained by fitting experimental data [65].

3. SIMULATION RESULTS

3.1 Waterflooding Simulations Scenarios

In order to achieve the objectives proposed in this work, different waterflooding simulations were conducted in three different model scenarios:

- 1) Sea water (SW) flooding scenario.
- 2) Low salinity water (LSW) flooding scenario.
- 3) Low salinity water (LSW) flooding scenario considering Adsorption processes.

The simulations are focused on evaluating the impact of fracture aperture distribution and fracture aperture on the final oil recovery when SW and LSW are injected in the fractured model. In the simulated injection scenarios, water is injected in an oil saturated rock. The gravity effects are neglected, and rock and fluids properties are described in Table 2. For the LSW scenario, the injected water is considered to have the same properties as for SW scenario. However, they are characterized by different set of relative permeabilities and capillary pressure curves, as it was described in **Section 2.3**. For the Adsorption model scenario, geochemical interactions are considered between the injected LSW and the rock matrix.

PROPERTY	VALUE	UNIT
Matrix Porosity	0,476	[\cdot]
Matrix Permeability	2,27e-15	[m 2]
Water density	1050	[kg/m 3]
Oil density	730	[kg/m 3]
Water viscosity	1,09	[cP]
Oil viscosity	0,92	[cP]

Table 2. Rock and fluid properties

A no-flow condition is defined in the boundaries parallel to the flow direction. Dirichlet boundary condition are assumed in the right edge of the model, whereby the pressure in the outflow is

maintained equal to 1 bar. In the left edge, we establish Neumann boundary conditions, which represents an injector well **Figure 9**.

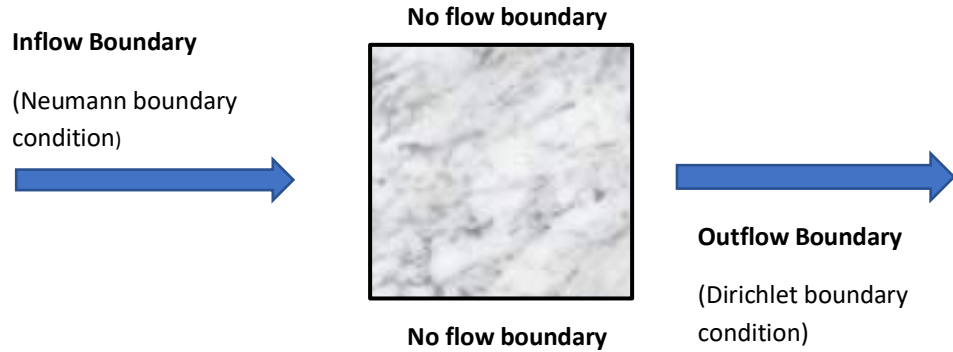


Figure 9. Schematic representation of the boundaries condition in the model

During the first simulations, water is injected at the left boundary of the domain, using fracture apertures of $10^{-3}[\text{m}]$, $10^{-4}[\text{m}]$, and $10^{-5}[\text{m}]$ in all the sector fractured models. In **Figure 10**, it is observed a snapshot of a front of constant saturation when an aperture fracture of $10^{-5}[\text{m}]$ is used, which correspond to a fracture permeability of $8.33 \times 10^{-13} \text{ m}^2$, according to **Equation 4**. The front of constant saturation reflects a uniform displacement of oil through the porous media, as a result of the relatively small permeability contrast between fracture and matrix ($\text{km} = 2.27 \times 10^{-15} \text{ m}^2$), which is not enough to produce an effect on sweep efficiency [66].

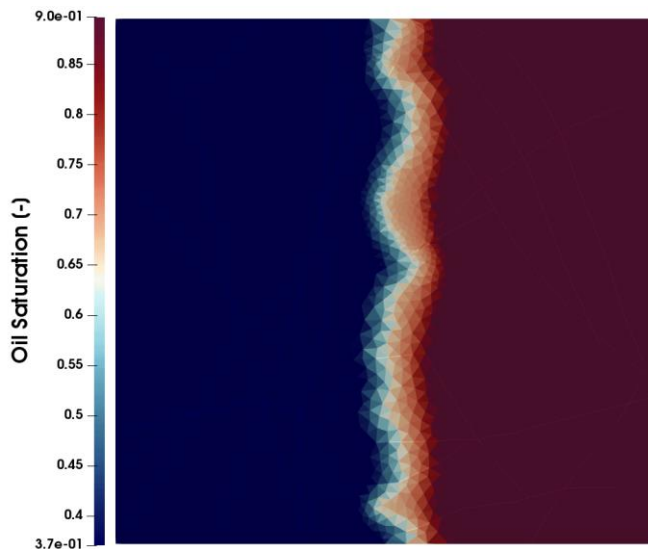


Figure 10. Snapshots of oil saturation front after 60 days of waterflooding using an injection rate of $1\text{e-}6 [\text{m}^3/\text{s}]$ and fracture aperture of $1\text{e-}5 [\text{m}]$

One of the objectives of this study is evaluated the effect of different fracture apertures on oil recovery efficiency with respect to injection rate. Since the effect of the apertures is only appreciable from fracture aperture values of $10^{-4}[\text{m}]$, we limit ourselves to simulations when fracture aperture is higher than $10^{-5}[\text{m}]$. Note that this consideration is valid only for the specific reservoir properties used in the simulations.

3.2 Sea Water Flooding Simulation

This model was evaluated under two different fracture aperture distribution patterns. We study the sensitivity of hydrodynamic simulations with respect to variations in aperture. We first show the results for a uniform aperture, which does not consider the impact of stresses. This first model was run with uniform values of fracture aperture of $10^{-4}[\text{m}]$, $5 \times 10^{-4}[\text{m}]$ and $1.5 \times 10^{-3} [\text{m}]$. In the second model, we assume the variable fracture aperture distribution according to the Barton-Bandis method described in **Section 2.2**.

3.2.1 Uniform Aperture Distribution

Fracture Pattern Effect on Fluid Flow Behavior

The simulations are performed considering a uniform fracture aperture of $10^{-4} [\text{m}]$ throughout the domain, using an injection rate of $1 \times 10^{-5} [\text{m}^3/\text{s}]$. The purpose of these simulations is to evaluate how the fracture pattern could affect the oil recovery during waterflooding.

Figure 11 shows that the presence of different fracture patterns (i.e. highly fractured, anisotropic and isolated) with different fracture orientation, fracture density and distribution can considerably affect the fluid flow behavior. Oil recovery and water cut (WCT) are evaluated as a function of time and pore volume of water injected, where WCT compares the volume of water produced with the total volume liquids produced (i.e. oil and water).

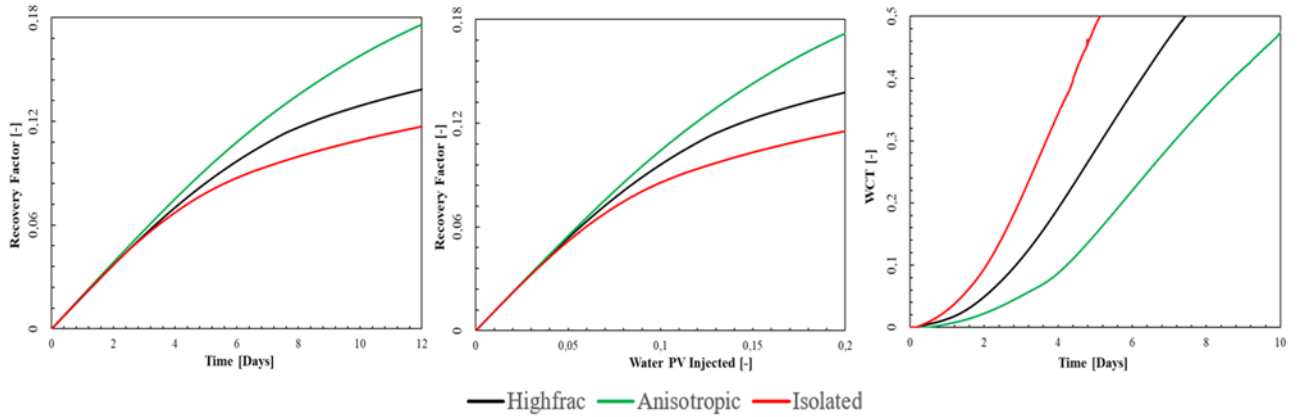


Figure 11. Recovery factor versus time (days) and Pore Volume (PV) of injected water using three different fracture sector model.

The results show that the waterflooding efficiency is higher for the anisotropic fracture pattern. Higher volume of oil is produced in less time by injecting lower volumes of water. **Figure 12** allows a better understanding of how the fluid flow behaves within the fracture-matrix pattern after 10 days of waterflooding for each sector model. In the highly fractured (**Figure 12a**) and isolated model (**Figure 12c**), the fracture distribution allows the water to have a preferential pathway through the medium producing early water production, while in the anisotropic model (**Figure 12b**), both the presence of vertically oriented fractures and the low degree of fracture connectivity with the horizontal fractures generate a more efficient oil sweep. Fracture flow become insignificant compare with flow within the porous matrix.

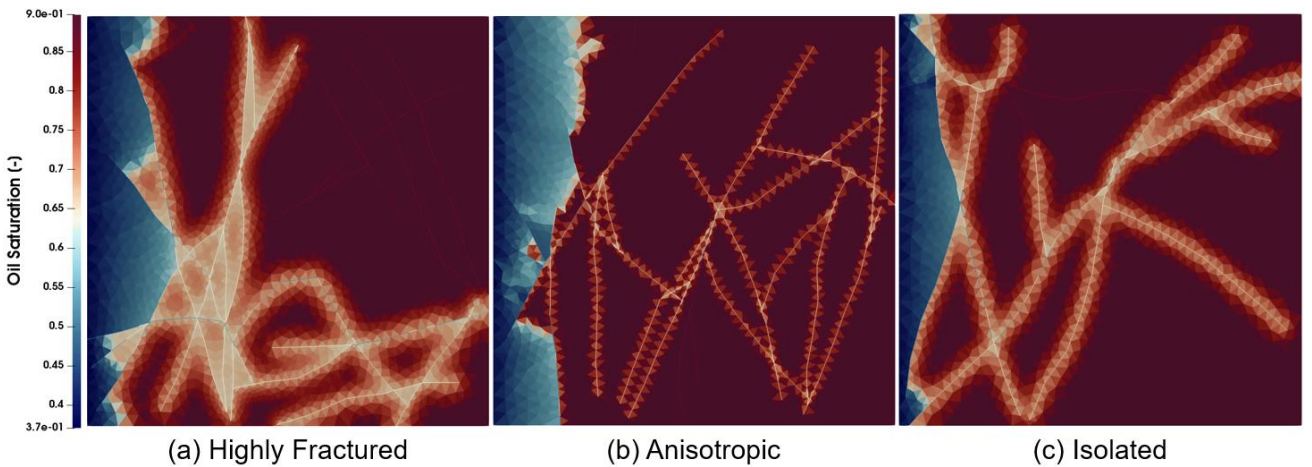


Figure 12. Snapshot of the fluid behavior in different fracture pattern models after 10 days of waterflooding.

Injection Rate Effect on Oil Recovery

To investigate the effect of injection rate in the waterflooding, a sensitivity analysis is performed by setting a uniform aperture value and using different injection rates in the highly fractured model. **Figure 13** shows the results of the simulations for a fracture aperture of 10^{-4} [m] and with injection rates of 1×10^{-6} [m³/s], 5×10^{-6} [m³/s] and 1×10^{-5} [m³/s].

The results from **Figure 13** indicate a gradual increasing in oil recovery as the injection rate increases. We can notice that higher injection rates lead to faster oil recovery using lower volumes of injected water. Injected water is imbibed in the matrix avoiding flow through the fracture's path. However, the water breakthrough is reached just few days after waterflooding initiate.

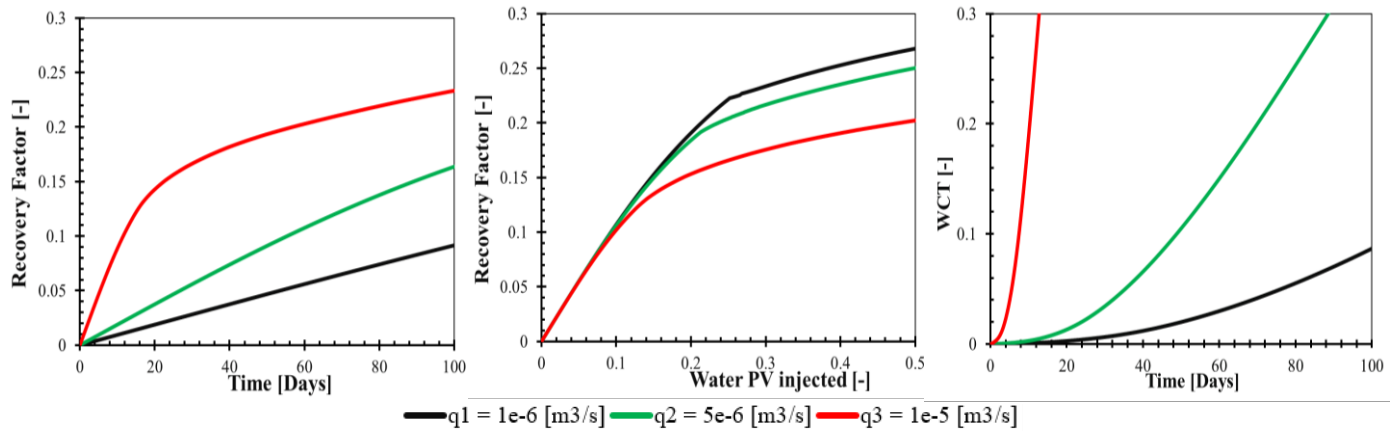


Figure 13. Recovery factor and WCT for waterflooding in the highly fractured model for a uniform aperture of 1×10^{-4} [m].

Fracture Aperture effect on Oil Recovery

In order to understand the impact of the aperture fracture on waterflooding processes, several simulations were run considering three scenarios by using the same injection rate but with a series of different fracture aperture values. **Figure 14** shows the behavior of oil recovery and water cut as a function of time, for aperture values of 1×10^{-4} [m], 5×10^{-5} [m] and 1×10^{-3} [m], using an injection rate of 1×10^{-5} [m³/s].

Note that the larger is the fracture aperture, the lower the waterflooding efficiency. The injected water will be channeled and flowed easily through fracture, leading to high water cuts at considerable

early stages of the injection. Moreover, it is observed that when the aperture is small, the oil sweep efficiency is greater. This is because there is no considerable contribution to flow by the fractures. Therefore, the fluid is displaced through the matrix, avoiding an early water breakthrough, and requiring lower volume of injected water.

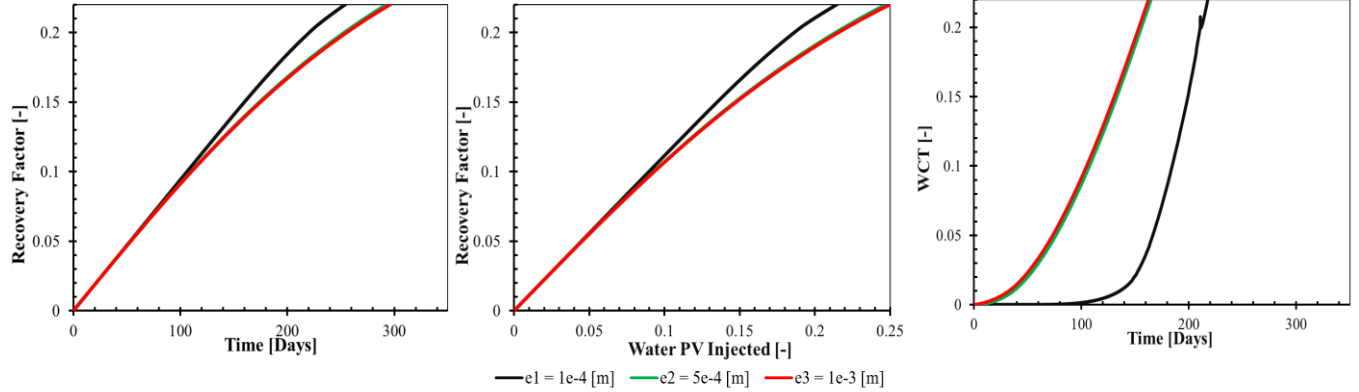


Figure 14. Recovery factor and WCT for waterflooding in the highly fractured model for uniform aperture of 1×10^{-4} [m], 5×10^{-4} [m] and 1×10^{-3} [m].

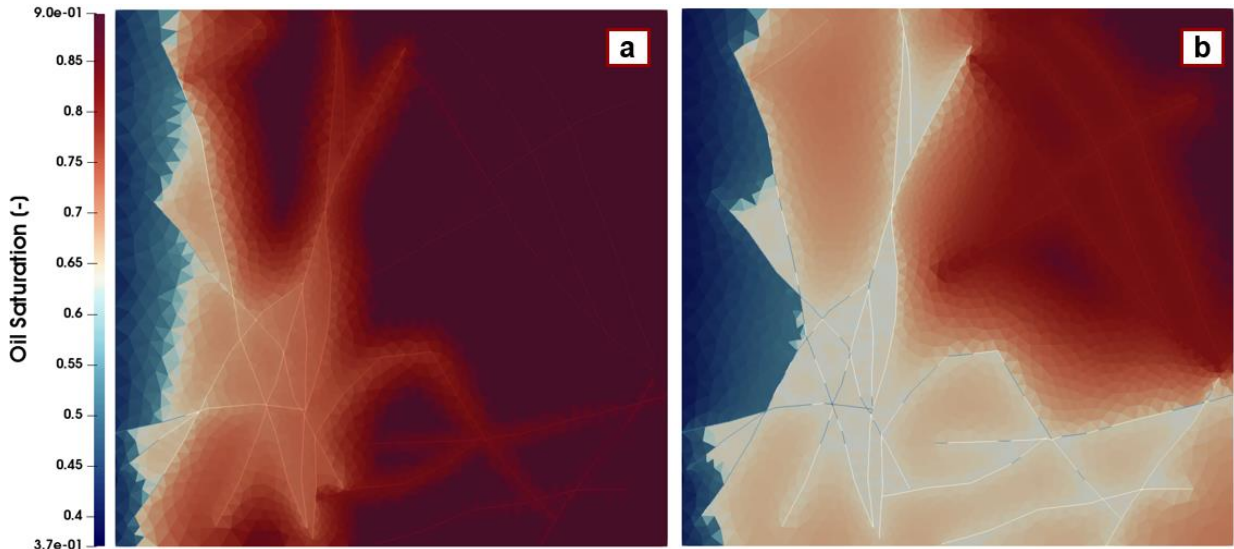


Figure 15. Snapshot of the fluid behavior in the highly fractured pattern model after 100 days of waterflooding.

In **Figure 15**, we can observe the snapshots of two simulated scenarios after 100 days of simulation. In scenario (a) with a fracture aperture of 1×10^{-4} [m], the waterfront moves more homogeneously through the porous medium with small water intrusion into the fractures. This leads to an efficient oil sweep in large part of the model section. On the other hand, in scenario (b), with a fracture

aperture of $1 \times 10^{-3} [\text{m}]$, the water quickly enters into the fractures. The water breakthrough is reached during the first days of waterflooding. As can be seen in the **Figure 15b**, there are sectors of the model that have not been efficiently swept, the injected water passes through the fractures leaving oil trapped.

3.2.2 Variable Aperture Barton-Bandis distribution

For this set of simulations, we consider that the domain has variable fracture apertures distribution, which are determined according to the Barton-Bandis model. The far-field stresses are set orthogonally to the model domain, with $\sigma_1 = 26.7 \text{ MPa}$ and $\sigma_3 = 10 \text{ MPa}$.

For the analysis of the orientation effect, the maximum principal stress (σ_1) is applied at two different angles α . One vertically orientated $\alpha = 0^\circ$ and, the second one, horizontally orientated $\alpha = 90^\circ$ (**Figure 6**). In both cases, the initial unstressed aperture E_0 is assumed to be $0.0015 [\text{m}]$. Where α indicates the angle of rotation of the far-field stress with respect to the Y and X axes, i.e. $\alpha = 0^\circ$, oriented in Y axes. In order to consider the impact of the stress and quantify aperture distribution for each network, simulations were conducted for all three sector models. **Figure 16** shows the fracture aperture distribution and the histograms of apertures frequency for the three sector models applying the Barton-Bandis approach. **Table 4** lists the corresponding values of average fracture aperture, average fracture permeability, and the fracture-matrix permeability ratio for each sector model, for the scenarios where the maximum principal stress is applied at $\alpha = 0^\circ$ and $\alpha = 90^\circ$.

	Unit	Highly Fractured		Anisotropic		Isolated	
		$\alpha = 0^\circ$	$\alpha = 90^\circ$	$\alpha = 0^\circ$	$\alpha = 90^\circ$	$\alpha = 0^\circ$	$\alpha = 90^\circ$
Avg. Fracture Aperture (e)	[mm]	0.87	0.73	0.97	0.64	0.87	0.73
Avg. Fracture Permeability (k_f)	[m ²]	6.71E-08	4.76E-08	8.26E-08	3.51E-08	6.86E-08	4.65E-08
k_f/k_m	[\cdot e+7]	29.5	20.9	42.8	15.4	38.5	31.8

Table 2. Average aperture and fracture permeability in the fractured sector models by applying Barton-Bandis model when maximum principal stress σ_1 is applied at $\alpha = 0^\circ$ and $\alpha = 90^\circ$

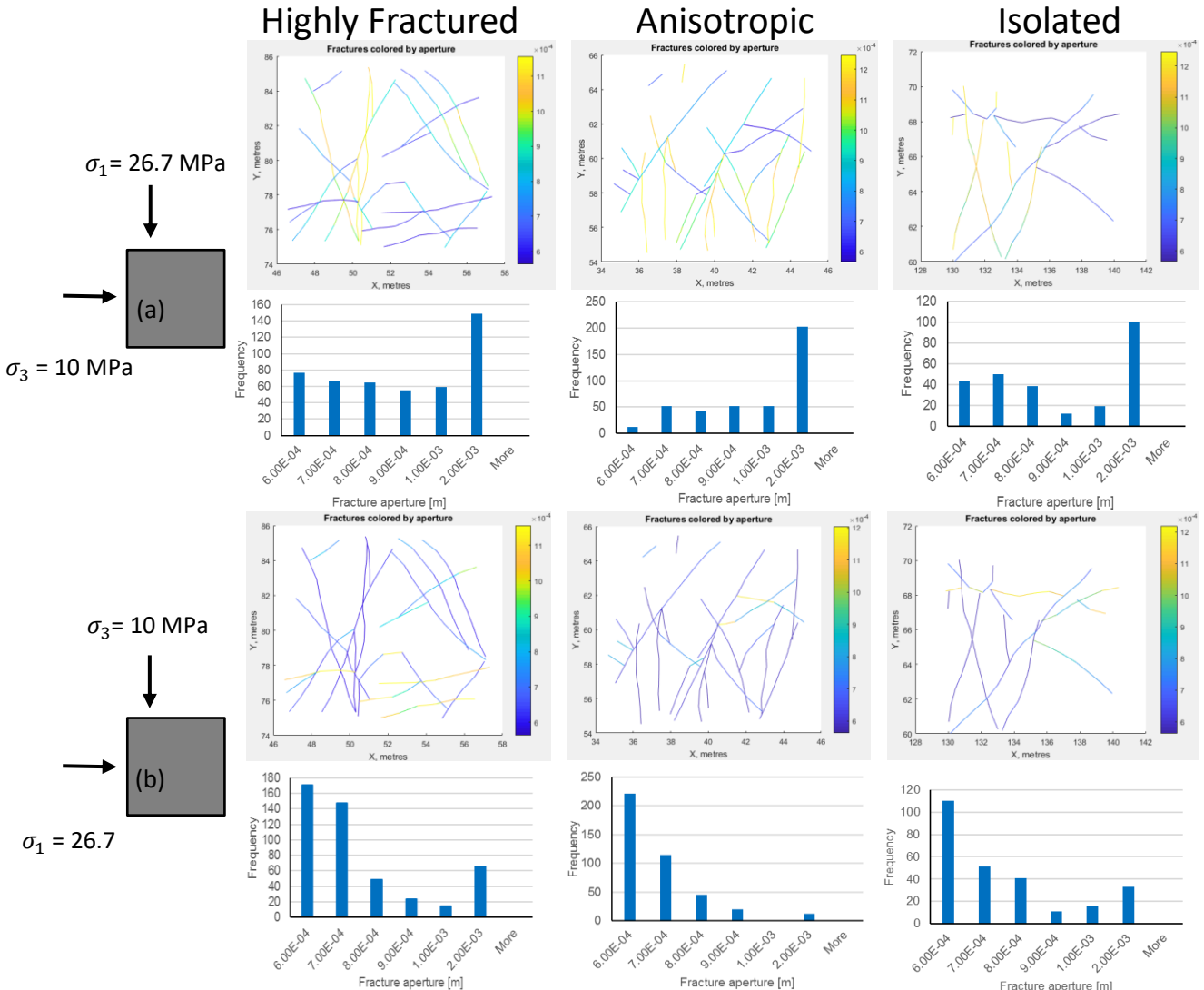


Figure 16. Fracture and frequency aperture distribution according to the orientation of the maximum stress applied in the fractured sector models.

With the change in orientation of the maximum stress applied σ_1 ($\alpha = 0^\circ$ and $\alpha = 90^\circ$), the fracture aperture distribution changes. Considering the highly fractured pattern, when the maximum stress is applied at $\alpha = 0^\circ$ (vertically) (Figure 16a), the highest value of stress aligns with the orientation of most of the fractures, producing larger apertures in the fractures that are vertically oriented. Therefore, this fracture aperture distribution cause channels for vertical flow. On the other hand, fractures in the case of $\alpha = 90^\circ$ (Figure 16b) are associated with smaller apertures, due to the fact that a stress load in $\alpha = 90^\circ$ tends to enhance the compression of vertically oriented fractures and therefore, reduces fractures apertures.

Notice that the average fracture permeability and fracture aperture is evidently much higher when the maximum principal stress is applied in the same orientation of most of the fracture, which in this specific case is in vertical direction. This is due to the geometrical anisotropy of the fracture pattern (**Table 3**), where most of the fractures are vertically oriented. As we can observe, the Barton and Bandis model allows fracture permeability to vary not only along fracture length, , but also in function of the fracture orientation.

Orientation Stress Effect on Oil Recovery

Consider the two scenarios, where the maximum principal stress (σ_1) induced is at $\alpha = 0^\circ$ and $\alpha = 90^\circ$. We compare these two scenarios using an injection rate of $1 \times 10^{-5} [\text{m}^3/\text{s}]$ in the x-direction, and in y-direction. **Figure 17** compares the simulation results of the two scenarios, evaluating recovery factor and WCT as a function of time and pore volumes of water injected for the anisotropic sector model. The dashed lines represent flow behavior in x-direction, while the solid lines show the trend of flow in y-direction.

In **Figure 17**, it can be observed that oil recovery is more efficient when waterflooding is in y-direction than in x-direction case with respect to time and pure volume of injected water. This effect can be related to a better conductivity between fractures in the case of x-direction as compared to the waterflooding in y-direction. As a result, in the case of waterflooding in x-direction, the injected water does not flow effectively through the matrix and a lower oil recovery is obtained.

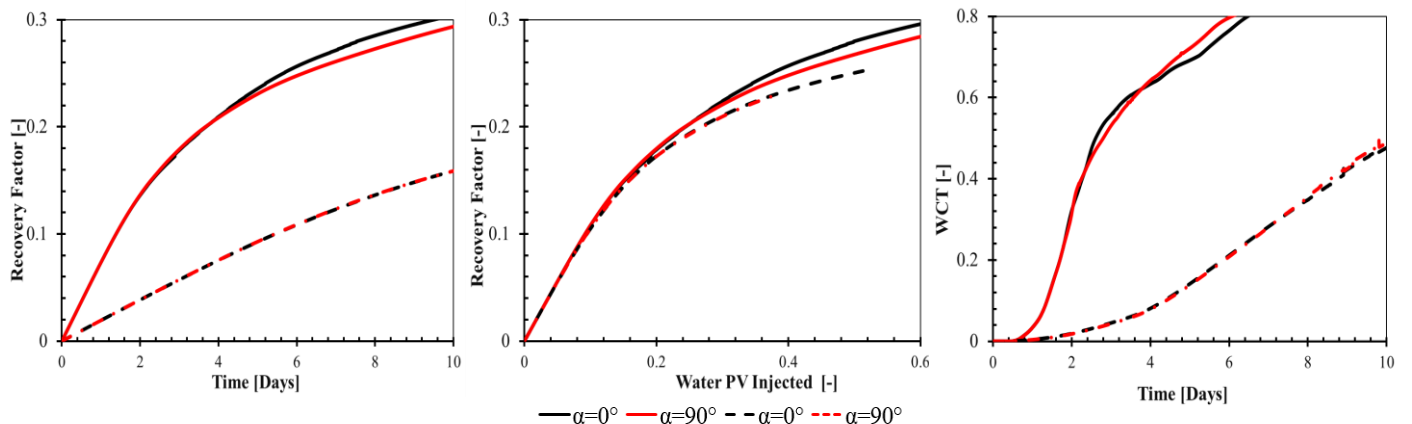


Figure 17. Oil recovery and WCT plot as a function of time for the anisotropic sector model, with injection rate of $1 \times 10^{-5} [\text{m}^3/\text{s}]$. applied in x and y direction.

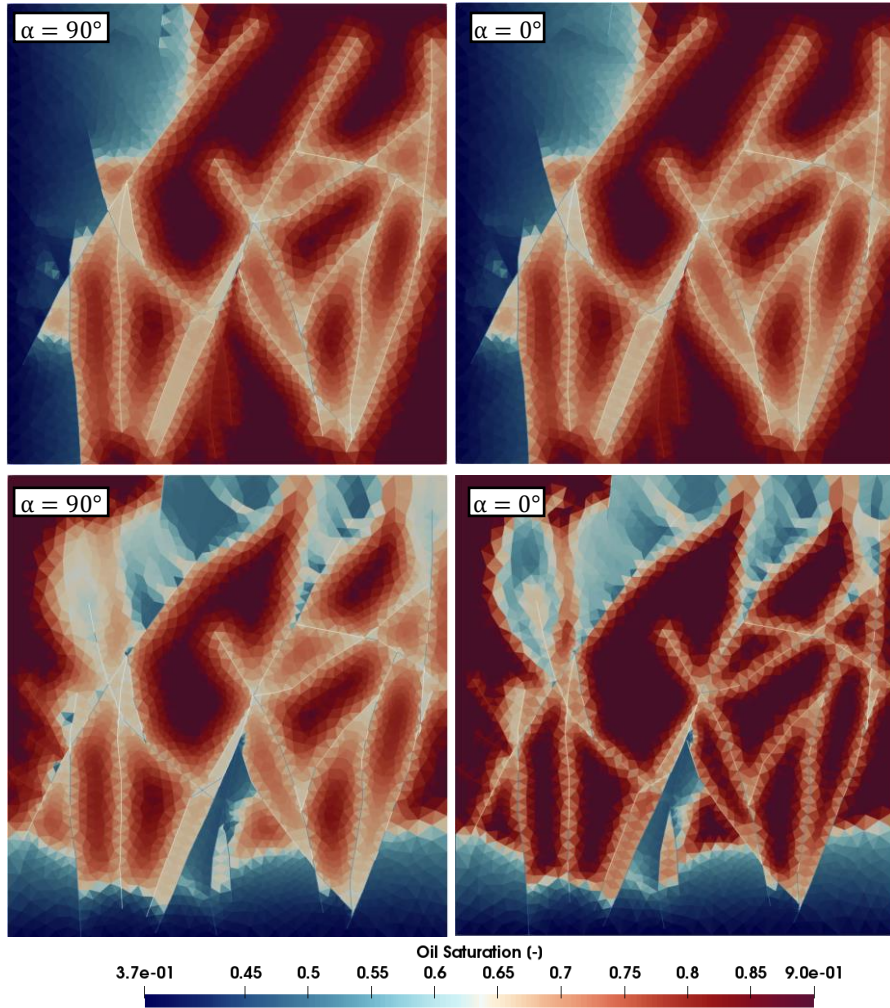


Figure 18. Snapshots of the anisotropic sector model in the x-direction (top) and y-direction (bottom) using injection rate of $1 \times 10^{-5} [\text{m}^3/\text{s}]$ after 4 days of waterflooding.

For the analysis of the effect of stress orientation, it can be seen that waterflooding in x-direction shows a low sensitivity to changes in the orientation of the principal stress applied. In both case ($\alpha = 0^\circ$ and $\alpha = 90^\circ$), the oil recovery curves are indistinguishable. This behavior can be explained by considering that for the anisotropic sector model, fractures are mostly vertical orientated but with a high horizontal conductivity. Therefore, water will be channeled through these preferential pathways, producing a decrease in sweep efficiency.

On the other hand, when water is injected in y-direction (solid lines in **Figure 17**), variation in the orientation of the principal stress applied seems to influence more the flow behavior. When the

maximum principal stress applied vertically ($\alpha = 0^\circ$) oil recovery is higher than in for the horizontal case ($\alpha = 90^\circ$). This is confirmed in **Figure 18** (bottom), which shows the snapshots of the two scenarios after 4 days of waterflooding in y-direction. In both scenarios, the injected water moves through fractures reaching the upper part of the model. However, fractures in the $\alpha = 90^\circ$ case tends to reduce oil sweeping efficiency in some areas which may be attributed to the more closed apertures under high horizontal stress. Contrary to $\alpha = 0^\circ$ case that allows to reach these areas. Therefore, higher volumes of oil are recovered in lower time.

3.2.3 Comparison between Uniform vs. Variable fracture aperture

In this section, we compare three different aperture distributions which are applied during the simulations in the fractured sector models: (1) Uniform aperture distribution with an aperture of 8.7×10^{-4} [m] and a fracture permeability of 6.71×10^{-8} [m²], and (2) the two Barton-Bandis scenarios when the maximum stress is applied at $\alpha = 0^\circ$ and $\alpha = 90^\circ$. The water injection rate is 1×10^{-5} [m³/s] in x direction. By comparing both cases, we aim to display the impact of the aperture distribution patterns on the oil recovery.

The uniform fracture model can be equivalent to a system of fractured rocks under isotropic conditions, where applied stresses are not high enough to affect the medium. On the other hand, with the Barton-Bandis model under anisotropic stress conditions, we compare the sensitivity of DFM using different fracture aperture distribution models, which allows to evaluate the effect of certain stress conditions in complex fracture networks. Fractures usually work as the main pathway for fluid flow in rocks. Moreover, the distribution of fluids in a fractured porous medium depends on the spatial distribution of fractures and fracture aperture, both of which can be affected by geomechanics conditions, as we can notice in **Figure 16**.

Figure 19 gives oil recovery from the system driven by injected water. The uniform aperture model tends to exhibit a higher oil recovery compare to the two Barton-Bandis models which produce less oil at the same time. However, the difference in oil recovery between each of three models increases

over time. **Figure 20** shows the evolution in time (20 days (top) and 40 days (bottom)) of the fluid in the highly fracture model for the three aperture distribution methods.

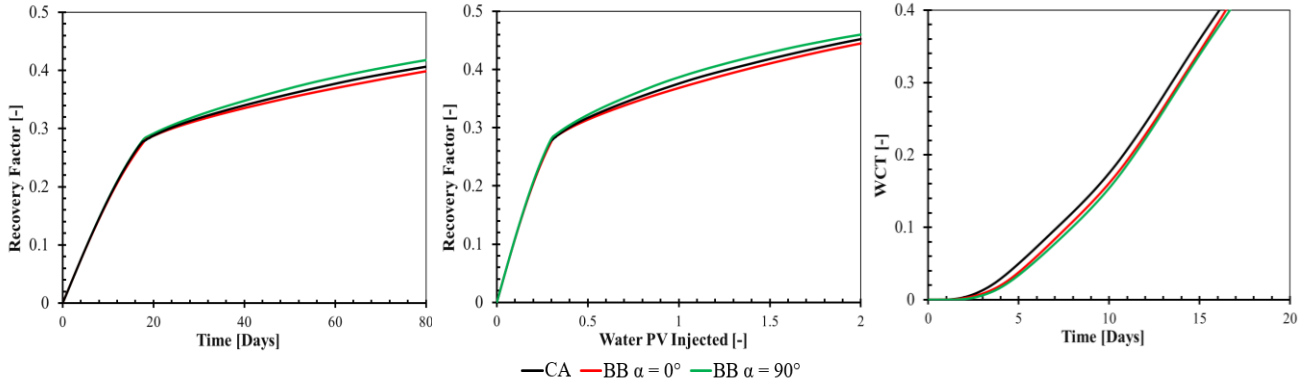


Figure 19. Oil recovery and WCT plot as a function of time for the highly fractured sector model, with injection rate of $1 \times 10^{-5} [\text{m}^3/\text{s}]$. applied in the constant aperture model and in the two Barton-Bandis scenarios ($\alpha = 0^\circ$ and $\alpha = 90^\circ$).

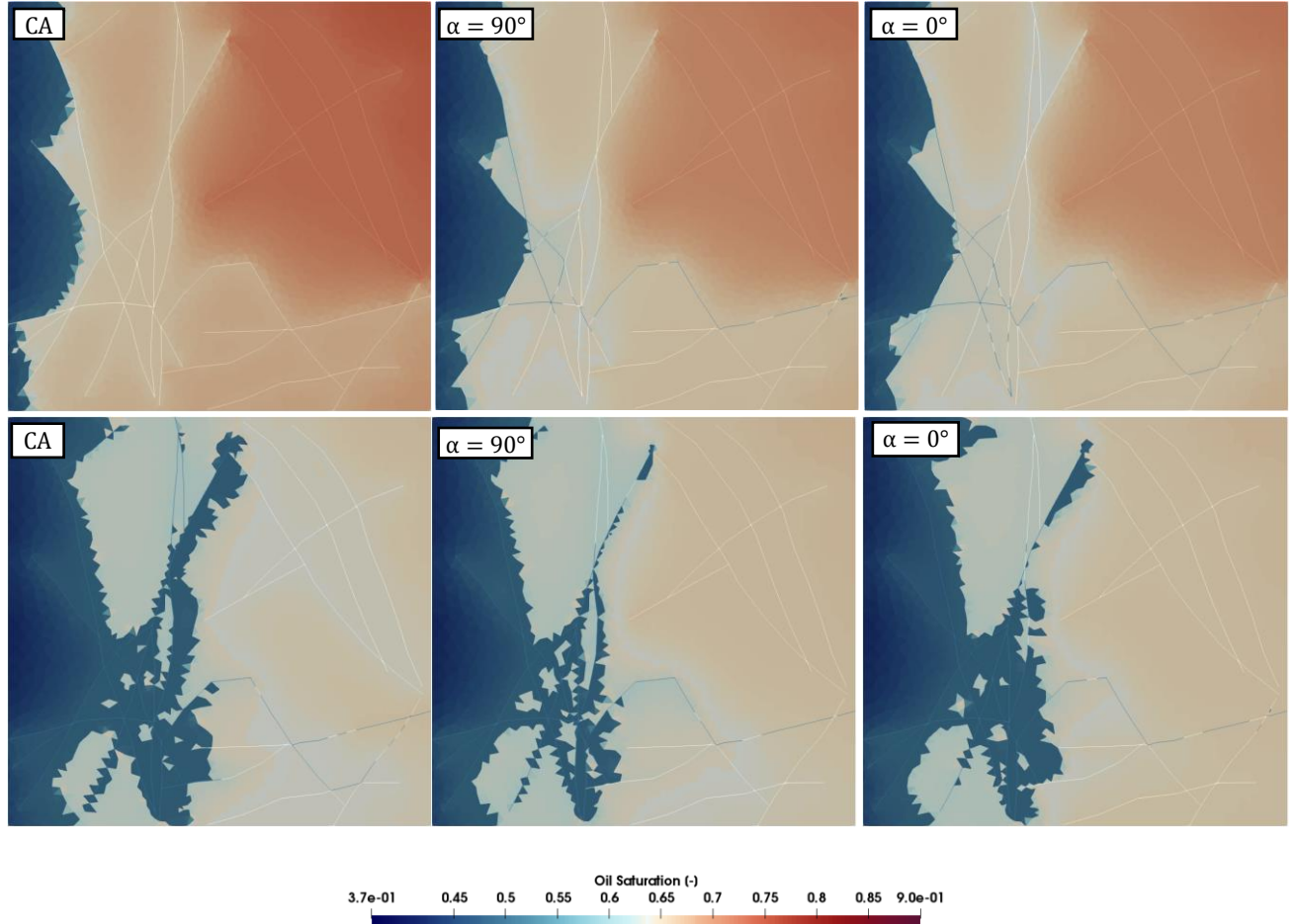


Figure 20. Snapshots of the highly fractured sector model using an injection rate of $1 \times 10^{-5} [\text{m}^3/\text{s}]$ for the constant aperture model and the two Barton-Bandis scenarios ($\alpha = 0^\circ$ and $\alpha = 90^\circ$). after 20 days (top) and 40 days (bottom) of waterflooding.

It can be seen that injected water penetrates through the porous matrix for all the cases, before gradually migrating into the fractures and finally water breakthrough is reached before the third day of injection (**Figure 19**). It seems that the stress condition with σ_1 applied at $\alpha = 90^\circ$ tends to exhibit more significant channelized flow than with σ_1 applied at $\alpha = 0^\circ$. For example, see the greater penetration of water into the fracture two thirds way down the left boundary in **Figure 20**(bottom). This is because the flow channels tend to align the direction of the maximum stress.

Matrix Permeability Effect on Fluid Flow

The effect of matrix-fracture permeability ratio in a fractured porous media is evaluated by considering a variable aperture distribution in the highly fractured sector model. **Figure 21** shows the variation of k_f/k_m by increasing the matrix permeability in 2 and 3 orders of magnitude, considering a constant fracture permeability k_f (6.71×10^{-8} [m²]) for all the sector models. The k_f/k_m contrast considered for each scenario is reported in the following table:

	k_m [m ²]	k_f/k_m [-]
0	2.27×10^{-15}	2.95×10^7
1	2.27×10^{-13}	2.95×10^5
2	2.27×10^{-12}	2.95×10^4

Table 3. Fracture permeabilities and fracture-matrix permeability ratio for different scenarios.

It can be noticed that the higher is the fracture-matrix permeability contrast, the lower is the oil recovery thus the flow is dominated by fractures. As shown in **Figure 22a**, fluid is predominantly transported through fracture zones, which leads to early water breakthrough. On the contrary, the increase in matrix permeability allows the injected water to flow through different zones in the fracture model, improving the oil sweeping, therefore oil recovery (**Figure 22b**).

The corresponding contribution of fracture permeability decreases as matrix permeability increases. The increase in oil recovery is the result of a higher penetration of injected water inside the fractured model pattern, allowing a more efficient oil displacement.

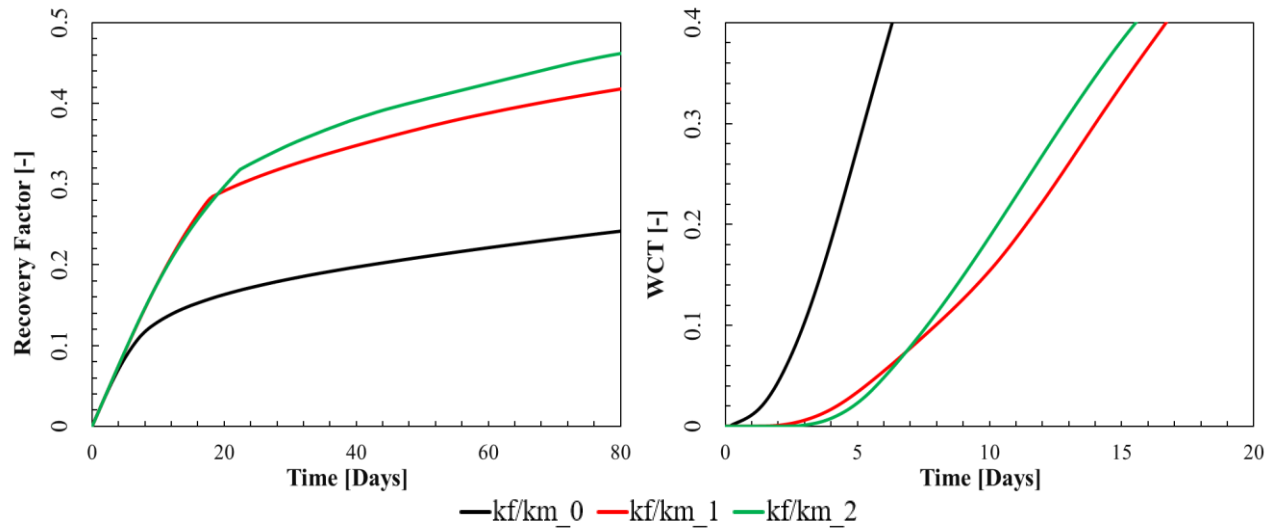


Figure 21. Oil recovery and WCT plot as a function of time for the highly fractured sector model, with injection rate of $1 \times 10^{-5} [\text{m}^3/\text{s}]$.for the Barton-Bandis scenarios when ($\alpha = 0^\circ$)

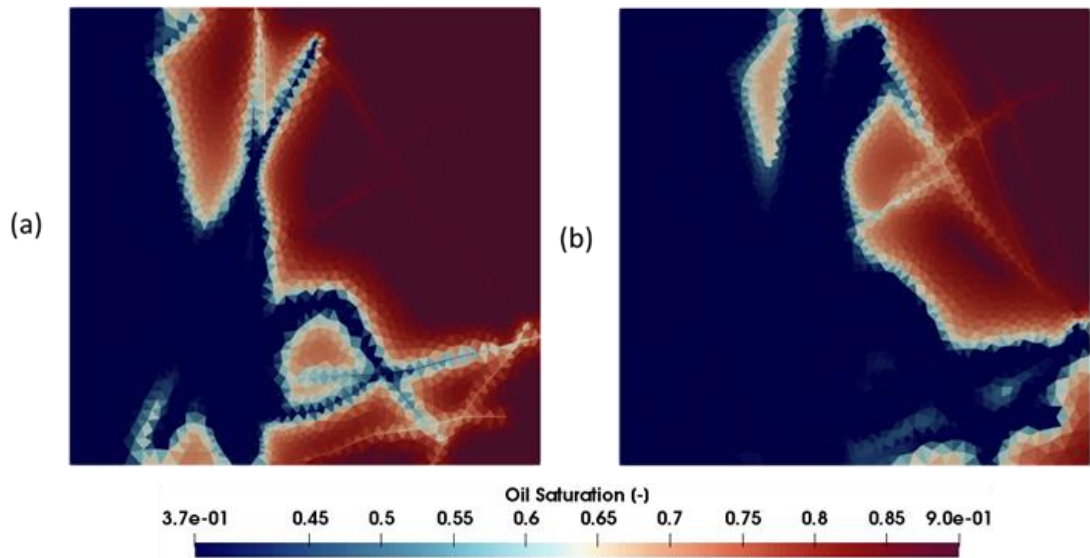


Figure 22. . Snapshots of the highly fractured sector model using an injection rate of $1 \times 10^{-5} [\text{m}^3/\text{s}]$. (a) for waterflooding simulations with high matrix/permeability contrast and (b) for the case of waterflooding simulations with low matrix/permeability contrast.

3.3 LSW Simulations

In this section, the LSW model is used to investigate the effect of some parameters such as water injection rate and fracture aperture on oil recovery during an LSW process, and also the comparison with SW flooding is presented.

Fractured and No Fractured Model Comparison

In order to evaluate the effect of fractures in LSW flooding, a set of simulations were performed with a water injection rate of 1×10^{-6} [m³/s]. **Figure 23** shows the results of a highly fractured sector model compared with a model without fractures. As expected, the model without fractures reaches the maximum oil recovery after 500 days of LSW flooding while the highly fractured model requires more than 900 days.

It should be pointed out that the two models have the same oil recovery factor until 170 days when water breakthrough time occurs in the fractured model. It means the water injected flows quickly through the fracture and by-passes the resident oil, leading to poor sweep efficiency and low recovery. However, by the time that water breakthrough (350 days) is reached in the no fractured model, most of the oil have been produced. This phenomenon can be observed in **Figure 24**, which shows the snapshot of the model after 170 days and 350 days of LSW flooding.

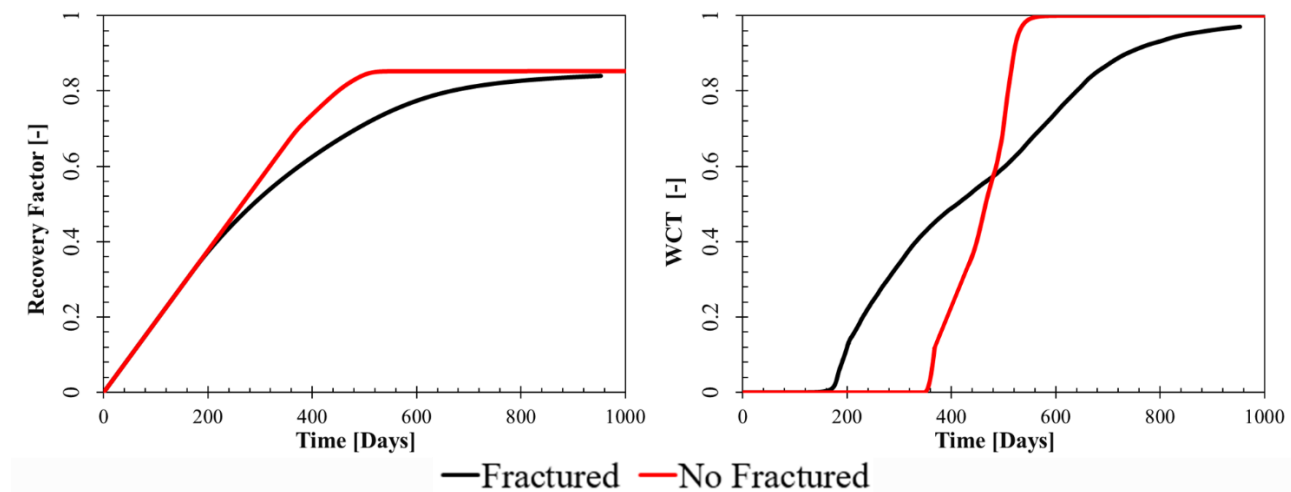


Figure 23. Recovery factors and WCT vs time for LSW flooding in a highly fractured model (black lines) and a model without fractures (red lines).

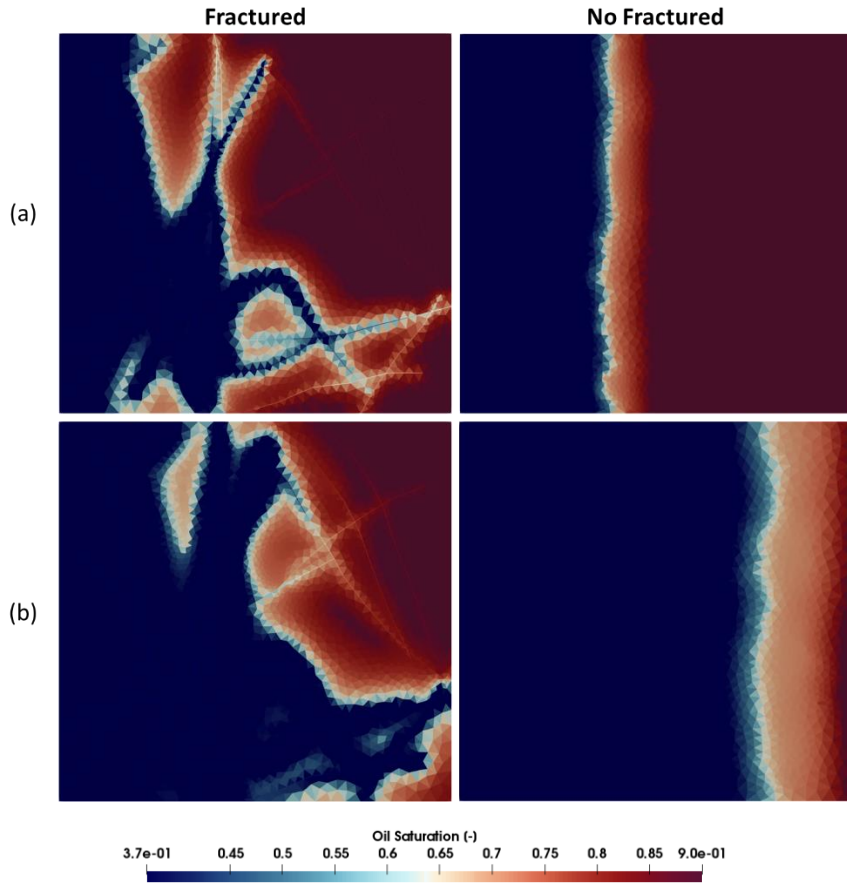


Figure 24. Snapshots of LSW flooding after 500 days for a highly fractured model (a) and a model without fractures.

Effect of Water Injection Rate on Oil Recovery

The model was run under injection rates of 1×10^{-6} [m³/s], 5×10^{-6} [m³/s] and 1×10^{-5} [m³/s]. **Figure 25** clearly shows the effect of injection rate on oil recovery during LSW flooding. Higher injection leads to less efficient oil sweeping and early water breakthrough. This result is also consistent with the results showed in the previous section for waterflooding processes.

Figure 25 indicates that breakthrough times for q₁, q₂, and q₃ injection rates happen at 142 days (0.23 PV), 17 days (0.14 PV), and 7 days (0.12 PV) after LSW flooding. This issue is also shown in the plot of water cut versus time, in which after these corresponding days, the amount of well water cut suddenly increased.

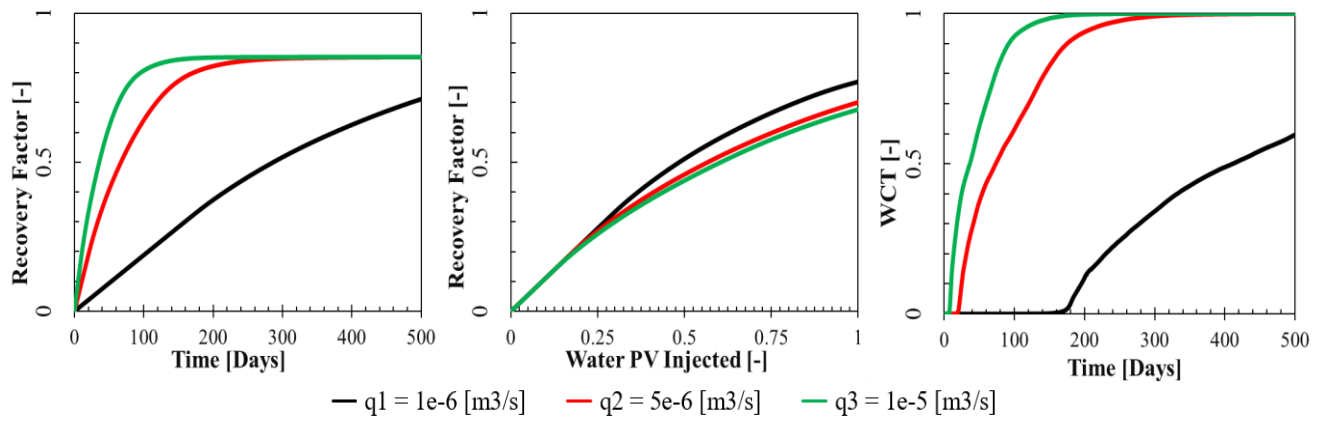


Figure 25. Recovery factors and WCT vs time for LSW flooding in a highly fractured under different injection flow rates.

SW flooding and LSW Flooding Comparison

An attempt is made to investigate the EOR effect when LSW flooding is applied in the reservoir. Using the same rock and fluid properties for the previously discussed cases, we compared oil recovery from the LSW flooding model with the SW flooding model. For the LSW model, there are considered three injected types of water with different salinity concentration compared with the injected SW. The injected waters are SW, a ten-times diluted SW (SWx10), a twenty-times diluted SW (SWx20), and a hundred-times diluted SW (SWx100).

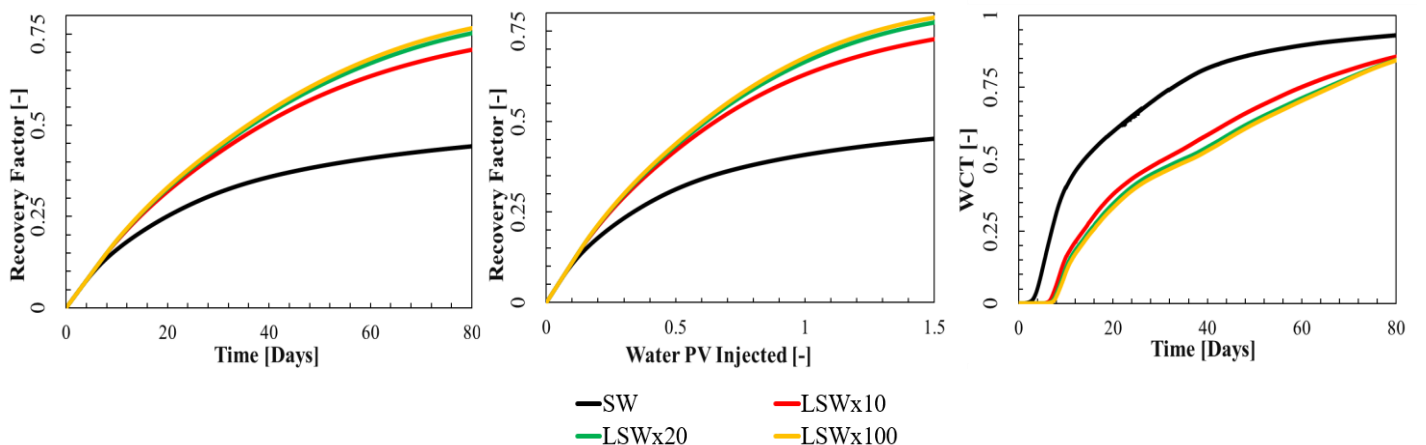


Figure 26. Recovery factors and WCT vs time for SW and LSW flooding in a highly fractured model.

Figure 26 shows the result of a set of simulation, which are run in a highly fractured sector model with a constant fracture aperture equal to $1 \times 10^{-4} \text{ [m]}$, and an injection rate of $1 \times 10^{-5} \text{ [m}^3/\text{s]}$. It can be seen that in all models, the oil recovery is the same until the water breakthrough time is reached,

producing a reduction in oil recovery efficiency. When the dissolution of SW increases, the water breakthrough times are delayed, and an increase of the oil sweep efficiency is observed. In the **Figure 26**, LSW models show a considerable improvement in oil efficiency after 40 days of flooding by 21.2%, 38.1% and 42.3% for the three models in comparison to the SW model.

3.4 LSW Simulations considering Adsorption Processes

In the previous sections, we established that during waterflooding simulations, the geochemical reactions between rock and water injected are not considered, which are expected to occur in LSW process as a result of a disturbance in the thermodynamic equilibrium [67]. In this section an attempt has been made to compare the effect of adsorption process on oil recovery during waterflooding simulations with respect to a no-adsorption model, which is the same model used for LSW simulations.

Figure 27 shows a comparison between two sets of waterflooding simulations. One set considering adsorption process between the rock surface and the injected water, and the second one, neglecting adsorption effects. Both sets of waterflooding simulations are implemented on the highly fractured model. These simulations were conducted using an injection rate of 1×10^{-5} [m³/s], and with a uniform fracture aperture of 1×10^{-4} [m].

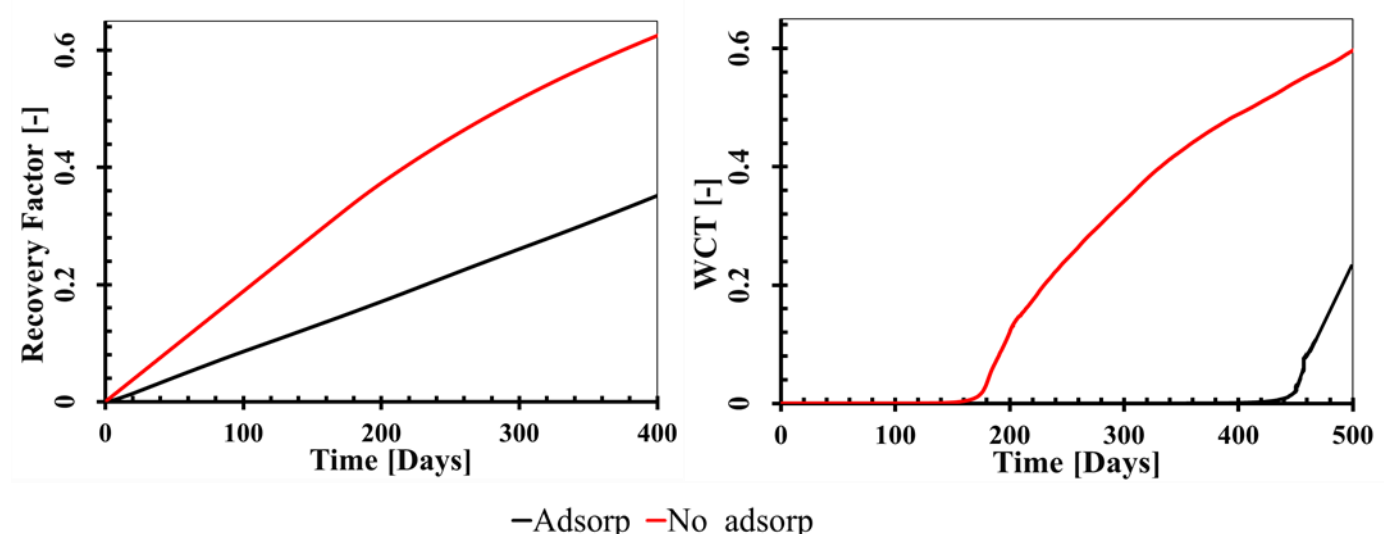


Figure 27. Recovery factors and WCT vs time for two set of simulation the adsorption and No adsorption model in the highly fractured sector model.

In the **Figure 27**, we can observe that adsorption simulations show a lower oil recovery during LSW process in comparison to no-adsorption simulations. In the adsorption simulation, oil recovery was about 10% of OOIP after 173 days of waterflooding (breakthrough time) while the no-adsorption simulation recovered 30% of OOIP by this time. It can be noticed that the water breakthrough times for both set of simulations differ in 249 days, with a breakthrough time of 173 days and 30% of OOIP in the no-adsorption model and 402 days and 30% of OOIP in the adsorption model. Therefore, more water injected ant time are required in order to reach the same oil recovery.

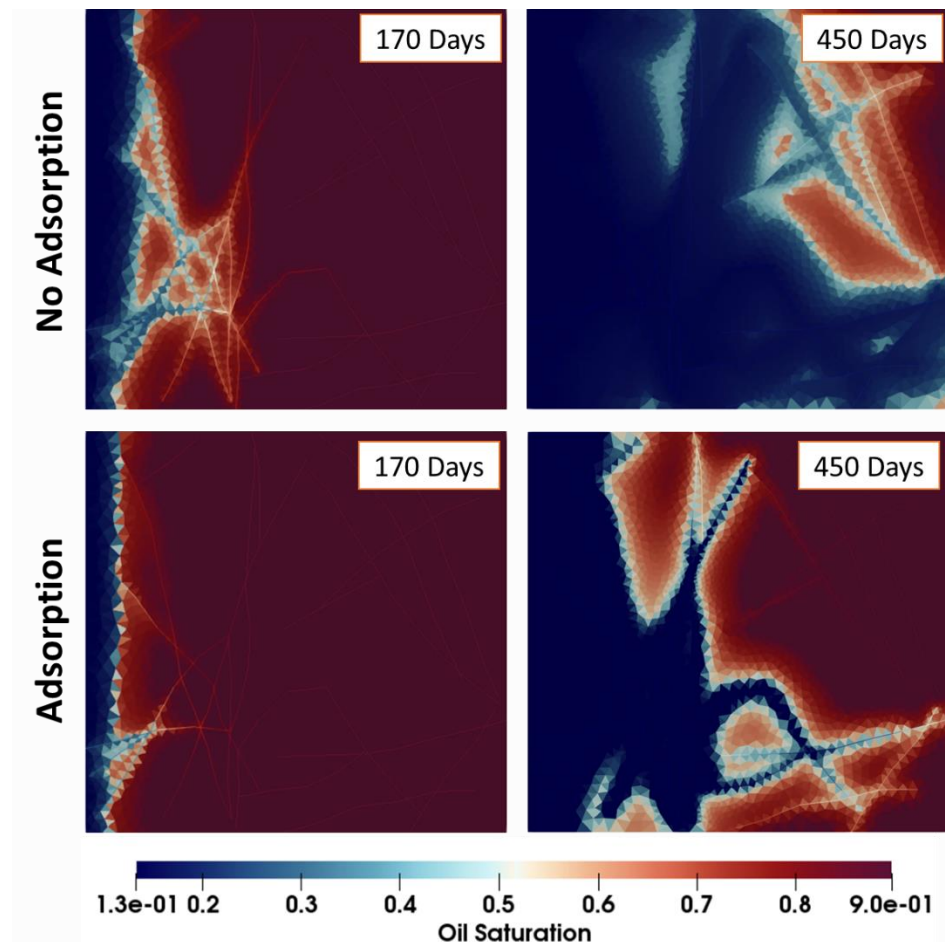


Figure 28. Snapshots of LSW flooding for two set of simulation the adsorption and No adsorption model in the highly fractured sector model after 170 and 470 days.

Figure 28 shows the snapshots of the two set of simulations at 170 days and 450 days after waterflooding, the saturation front of the adsorption model has a retardation with respect to the no-adsorption model, which is consistent with the mathematical model presented in **Section 2.4**. In

addition, it can be observed that after water breakthrough, the no-adsorption model shows a better hydrocarbon sweep efficiency. There is a higher penetration of water through the sector model allowing an efficient oil displacement. On the other hand, in the adsorption model most of the injected water scape from the path provide by fractures.

Sensitivity Analysis of Adsorption Parameters

After the comparative analysis between the adsorption model and the no-adsorption model, this part of the work aims at studying the different parameters that affect the adsorption model during LSW flooding simulations. As it was outline in **Section 2.4**, in order to model the impact of adsorption on oil displacement during waterflooding in a porous media, the adsorption isotherm models are an essential tool to describe the equilibrium relationship between the solute in solution and the adsorption surface [68]. Therefore, the oil recovery is study by making a sensitivity analysis of waterflooding simulations with respect to changes in the key adsorption parameters.

The proposed adsorption model involves certain number of parameters. Three sensitivity analyses were performed to understand the relevance of the adsorption parameters in improving oil recovery. Firstly, γ_1 is chosen to vary from a value of 1 to 50, and 100 while the γ_2 and n remain constant and equal to 0 and 1, respectively. In the second analysis, γ_2 is varied with values from 0 to 50, keeping γ_1 and n constant and equal to 1. Finally, the third part of the analysis intent to study the effect of n on the adsorption model. Parameter n varies from 1 to 50, while the γ_1 and γ_2 remain constant and equal to 1 and 0, respectively. **Table 6** shows a summary of the cases and evaluated parameters.

Fixed Values	Case	Sensitivity
$\gamma_2 = 0$ $n = 1$	Base	$\gamma_1 = 1$
	S2	$\gamma_1 = 50$
	S3	$\gamma_1 = 100$
$\gamma_1 = 1$ $n = 1$	S4	$\gamma_2 = 1$
	S5	$\gamma_2 = 10$
	S6	$\gamma_2 = 50$
$\gamma_1 = 1$ $\gamma_2 = 0$	S7	$n = 10$
	S8	$n = 50$

Table 4. Summary of the sensitivity cases and adsorption parameters values

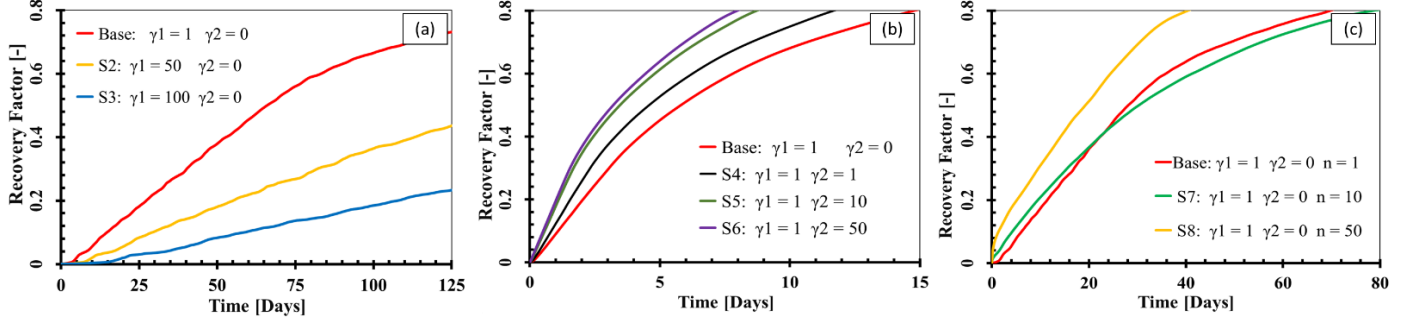


Figure 29. Recovery factors vs time for the sensitivity analysis of the adsorption model in the highly fractured sector model.

Figure 29a compares the oil recovery curves obtained by changing the reaction parameters γ_1 . It was observed that increasing the values of γ_1 from 50 to 100, the oil recovery improves from 25 to 65% after 50 days of waterflooding simulation. **Figure 29b**, a similar behavior is observed. The results show that as the adsorption parameters γ_2 increases oil recovery increases. In **Figure 29c**, we can observe that the sensitivity analysis of oil recovery when the adsorption parameter n varies from 1 to 10, initially, shows an increase in oil recovery, however after the water cut point is reached the behavior changes and the oil recovery is lower compared to the case where n is equal to 1.

CONCLUSIONS

Using a numerical DFM model, a fluid flow behavior study was performed on a fractured carbonate outcrop model. The objective of the thesis was to evaluate the impact of a fractured porous media on oil recovery, when sea water and low salinity water is injected.

Based on the simulation results, the following conclusions can be drawn:

- ✓ For simulations with fracture apertures lower than 1×10^{-5} [m], fractures have a negligible impact on fluid flow considering the specific reservoir properties of the model. Water saturation front is uniform and oil displacement has a piston-like behavior.
- ✓ By using fracture networks with different fracture distribution, locations, lengths and apertures, it was demonstrated that fluid flow in porous media is clearly influenced by the connectivity between the fractures. Changing size and spatial distribution produce a fracture network connectivity which is different in each sector model. In the case of fracture sector models with direct connectivity between inflow and outflow boundaries. Water breakthrough occurs at early times of water flooding, leading to a poorly oil sweeping. In addition, fracture orientation plays an important role in fluid behavior. As long as there is not communication between the boundaries of the model, the effect of changing orientation of the application of the principal stress is negligible.
- ✓ If fractures are aligned with the flow direction , they contribute more to flow.
- ✓ It was studied, the impact of stress on fluid flow through fractured porous media, based on the orientation of fractures. For fracture patterns that have a unique orientation set, the aperture fracture distribution display one defined peak. However, in the case of fracture patterns with different orientation sets, it was observed different peaks according to each set.

- ✓ Using Barton-Bandis, as a method for modeling the fracture aperture distribution of a porous media subject to geomechanical effects, it was studied the role of varying in stress state of fracture model in changing the global conductivity of the domain. The model suggests a linkage between the orientation of the far-field maximum principal stress applied and the orientation of the fractures. If the maximum stress applied is align with the fracture orientation, higher is the fracture aperture, therefore, the fractures tend to exhibit more significant channelized flow, and a greater water penetration through fractures.

- ✓ Oil recovery is influenced by the fracture-matrix permeability. As K_f/K_m ratio reduces the oil displacement efficiency increases. High permeable fractures provide a path for escape for fluids, therefore, in waterflooding process, the fracture transport will transport most of the injected water reducing oil displacement efficiency.

- ✓ From simulations between the adsorption and no adsorption model, it is confirmed a retardation in the water saturation front. It was observed that adsorption model shows a water saturation front with a slower displacement compared to the no adsorption model, resulting in lower oil recovery.

- ✓ Adsorption model is characterized by different adsorption isotherm curve. These isotherms are in function of some parameters which represent the capability of the medium to adsorb. Using different set of simulations, a sensitivity analysis was developed to study the effect on fluid flow. It was determined a direct relation between adsorption parameters and oil recovery efficiency. As these adsorption parameters increase a lower oil recovery efficiency is exhibit during waterflooding simulations.

References

- [1] T. BRATTON, "Characterization of Fractured Reservoirs: The nature of naturally fractured carbonate reservoirs," Schlumberger, Denver, Colorado, 2010.
- [2] A. A. YOUSEF, J. LIU and G. BLANCHARD, "SmartWater flooding: Industry's first field test in carbonate reservoirs," *SPE*, 2012.
- [3] M. MUSKAT, *Physical Principles Of Oil Production*, New York: McGraw-Hill Book Company, 1949.
- [4] A. MAI and A. KANTZAS, "Heavy Oil Waterflooding: Effects of Flow Rate and Oil Viscosity," *Journal of Canadian Petroleum Technology*, vol. 48, no. 03, January 2007.
- [5] F. CIVAN, "CHAPTER 19 - INJECTIVITY OF THE WATERFLOODING WELLS," in *Reservoir Formation Damage*, Gulf Professional Publishing, 2007, pp. 775-813.
- [6] J. UDY, B. HANSEN and S. MADDUX, "Review of Field Development Optimization of Waterflooding, EOR, and Well Placement Focusing on History Matching and Optimization Algorithms," *PROCESSES*, 27 June 2017.
- [7] L. W. LAKE, "Enhanced Oil Recovery," New Jersey, Prentice Hall, 1989, pp. 314-353.
- [8] J. UDY , B. HANSEN and S. MADDUX, "Review of Field Development Optimization of Waterflooding, EOR, andWell Placement Focusing on History Matching and Optimization Algorithms," *Processes*, vol. 05, no. 03, June 2017.
- [9] G. TANG and N. MORROW, "Salinity, temperature, oil composition and oil recovery by waterflooding," *SPE Reservoir Engineering*, pp. 169-276, 1997.
- [10] NASRALLA, RAMEZ A; MAHANI, HASSAN; VAN DER LINDE, HILBERT A;, "Low Salinity Waterflooding for a Carbonate Reservoir: Experimental Evaluation and Numerical Interpretation," *Journal of Petroleum Science and Engineering*, pp. 640-654, 2018.
- [11] M. DERKANI, A. FKETCHER and W. ABDALLAH, "Low Salinity Waterflooding in Carbonate Reservoirs: Review of Interfacial Mechanisms," *Colloids Interfaces*, no. Colloids and Interfaces in Oil Recovery), 2018.

- [12] T. PUNTERVOLD, S. STRAND and T. AUSTAD, "Coinjection of Seawater and Produced Water to Improve Oil Recovery from Fractured North Sea Chalk Oil Reservoirs," *Energy Fuels*, pp. 2527-2536, 2009.
- [13] S. STRAND, T. AUSTAD and T. PUNTERVOLD, "Is Wettability Alteration of Carbonates by Seawater Caused by Rock Dissolution?," in *International Symposium of the Society of Core Analysts*, Netherlands, 2009.
- [14] W. ALAMERI, T. TEKLU and R. GRAVES, "Wettability Alteration of Carbonates by Seawater," in *SPE Asia Pacific Oil Gas Conference*, Adelaide, Australia, 2014.
- [15] HIORTH, A; CATHLES, L M; MADLAND, M;, "The Impact of Pore Water Chemistry on Carbonate Surface Charge and Oil Wettability," *Transport in Porous Media*, vol. 85, no. 11-21, 2010.
- [16] P. ZHANG, M. TWEHEYO and T. AUSTAD, "Wettability alteration and improved oil recovery by spontaneous imbibition of seawater into chalk: Impact of the potential determining ions Ca, Mg, and SO₄," *Colloids and Surfaces A: Physicochemical and Engineering Aspects*, vol. 301, no. 1-3, pp. 199-208, 2007.
- [17] S. M. MOHAMMAD, P. OMIDVAR and F. NAEIMI, "Salinity of injection water and its impact on oil recovery absolute permeability, residual oil saturation, interfacial tension and capillary pressure," *Egyptian Journal of Petroleum*, vol. 26, pp. 301-312, 2016.
- [18] A. LAGER, J. WEBB and C. J. BLACK, "Low salinity oil recovery - An experimental investigation," *Petrophysics*, vol. 49, no. 1, pp. 28-35, 2008.
- [19] C. DANG, L. NGHIEM and Z. CHEN, "Modeling Low Salinity Waterflooding: Ion Exchange, Geochemistry and," *spe 166447*, 2013.
- [20] D. DING, N. FARAH and B. BOURBIAUX, "Simulation of Matrix/Fracture Interaction in Low-Permeability Fractured Unconventional Reservoirs," *SPE*, vol. 23, no. 04, pp. 182608-PA, 2018.
- [21] N. R. COUNCIL, "Chapter 6. Field-Scale Flow and Transport Models," in *Rock Fractures and Fluid Flow: Contemporary Understanding and Applications* , Washington, DC, The National Academies Press, 1996, pp. 307-403.

- [22] D. GLÄSER, R. HELMIG and B. FLEMISH, "A discrete fracture model for two-phase flow in fractured porous media," *Advances in Water Resources*, vol. 110, pp. 335-348, 2017.
- [23] I. BERRE, F. DOSTER and E. KEILEGAVLEN, "Flow in fractured porous media: A review of conceptual models and discretization approaches," arXiv:1805.05701v1, 2018.
- [24] S. GEIGER and S. MATTHÄI, "What can we learn from high-resolution numerical simulations of single- and multi-phase fluid flow in fractured outcrop analogues?," *Advances in the Study of Fractured Reservoirs*, vol. 374, no. Geological Society of London, 2012.
- [25] A. KOESTLER and K. REKSTEN, "Fracture-network 3D characterization in a deformed chalk reservoir analogue -- the Laegerdorf case," *SPE*, vol. 10, no. 3, pp. doi:10.2118/28728-PA, 1995.
- [26] A. KOESTLER and K. REKSTEN, "Fracture-Network 3DCharacterization in a Deformed Chalk Reservoir Analogue - The Lägerdorf Case," *SPE*, 1995.
- [27] A. G. KOESTLER and W. U. EHRMANN, "Fault patterns in the calcareous overburden of a salt diapir: Laegerdorf, NW Germany," *geo-recon*, vol. N. Jb. Geol. Paläont. Mh, pp. 555-569, 1986.
- [28] A. G. KOESTLER and W. U. EHRMANN, "Fractured Chalk Overburden of a Salt Diapir Lägerdorf, NW Germany - Exposed Example of a Possible Hydrocarbon Reservoir," in *Dynamical Geology of Salt and Related Structures*, Orlando, Florida, Academic Press, 1987, pp. 457-477.
- [29] M. J. WELCH, C. SOUQUE and R. K. DAVIES, "Using Mechanical Models to Investigate the Controls on Fracture Geometry and Distribution in Chalks," in *Fundamental Controls on Fluid Flow in Carbonates: Current Workflows to Emerging technologies*, London, The Geological Society, 2015, pp. 281-294.
- [30] D. HEALY, R. E. RIZZO, D. G. CORNWELL and N. FARRELL, "FracPaQ: A MATLAB™ toolbox for the quantification of fracture patterns," *Journal of Structural Geology*, vol. 95, pp. 1-16, 2017.
- [31] N. ANDRIANOV and H. M. NICK, "Modeling of Waterflood Efficiency Using Outcrop-Based Fractured Models," *ELSEVIER*, 2019.

- [32] D. TIAB and E. C. DONALDSON, "Naturally Fractured Reservoirs," in *Petrophysics: Theory and practice of Measuring Reservoir Rock and Fluid Transport Properties*, ELSEVIER, 2015.
- [33] C. MOORE and W. WADE, "Natural Fracturing in Carbonate Reservoirs," in *Carbonate Reservoirs: Porosity and Diagenesis in a Sequence Stratigraphic Framework*, ELSEVIER, 2013, pp. 285-300.
- [34] E. GAMBOA and J. SUN, "Reducing Uncertainties of Fracture Characterization on Production Performance by Incorporating Microseismic and Core Analysis Data," *Society of Petroleum Engineers*, 2016.
- [35] G. D. AVANSI, C. MASCHIO and D. J. SHIOZER, "Simultaneous history matching approach using reservoir-characterization and reservoir-simulation studies," *SPE Reservoir Evaluation & Engineering*, vol. 19, no. 04, 2016.
- [36] N. BARTON and S. BANDIS , "Some Effects of Scale on the Shear Strength of Joints," *International Journal of Rock Mechanics and Mining Sciences & Geomechanics Abstracts*, vol. 17, pp. 69-73, 1980.
- [37] M. A. DIPPENAAAR and J. LOUIS VAN ROOY, "On the Cubic Law and Variably Saturated Flow Through Discrete Open Rough-Walled Discontinuities," *International Journal of Rock Mechanics Mining Science*, vol. 89, pp. 200-211, 2016.
- [38] S. C. BANDIS, A. C. LUMSDEN and N. R. BARTON, "Fundamentals of Rock Joint Deformation," *International Journal of Rock Mechanics and Mining Sciences* , vol. 20, pp. 249-268, 1983.
- [39] N. BARTON, "Modelling Rock Joint Behaviour from In Situ Block Test: Implications for Nuclear Waste Repository Design," in *Office of Nuclear Waste Isolation*, Columbus, Ohio, 1982.
- [40] S. AZIZMOHAMMADI and S. MATTHAI, "Is the permeability of naturally fractured rocks scale dependent?," *Water Resources Research*, vol. 53, no. 9, pp. 8041-8063, 2017.
- [41] R. R. HILLIS and E. J. NELSON, "In Situ Stresses in the North Sea and their Applications: Petroleum Geomechanics from Exploration to Development," in *Petroleum Geology: North-West Europe and Global Perspectives—Proceedings of the 6th Petroleum Geology*, London, 2005.

- [42] K. TERZAGHI, "Principles of Soil Mechanics: A Summary of Experimental Studies of Clay and Sand," *Engineering News-Record*, vol. 95, no. 19, pp. 742-746, 1925.
- [43] P. JAPSEN, "Regional Velocity-Depth Anomalies, North Sea Chalk: A Record of Overpressure and Neogene Uplift and Erosion," *Petroleum Geoscience*, vol. 82, no. 11, p. 2031–2074, 1998.
- [44] D. T. SNOW, "A Parallel Plate Model of Fractured Permeable Media. University of California Berkeley," *Ph.D. Thesis, Univ. of California*, 1965.
- [45] P. A. WITHERSPOON, J. S. WANG, K. IWAI and J. E. GALE, "Validity of Cubic Law for Fluid Flow in a Deformable Rock Fracture," *Water Resources Research*, vol. 16, pp. 1016-1024, 1980.
- [46] N. BARTON , S. BANDIS and K. BAKHTAR, "Strength Deformation and Conductivity Coupling of the Rock Joints," *International Journal Rock Mechanics and Mining Sciences*, vol. 22, no. 3, pp. 121-140, 1985.
- [47] K. BISDOM, G. BERTOTTI and H. NICK, "The impact of in-situ stress and outcrop-based fracture geometry on hydraulic aperture and upscaled permeability in fractured reservoirs," *Tectonophysics*, vol. 690, pp. 63-75, 2016.
- [48] A. OBEYSEKARA, Q. LEI, P. SALINAS and D. PAVLIDIS, "Modelling stress-dependent single and multi-phase flows in fractured porous media based on an immersed-body method with mesh adaptivity," *Computer and geotechnics*, vol. 103, pp. 229-241, 2018.
- [49] Y.-S. Wu, "Numerical Model and Formulation," in *Multiphase Fluid Flow in Porous and Fractured Reservoirs*, Colorado, USA, Gulf Professional Publishing, 2016, pp. 49-59.
- [50] R. A. NELSON, *Geologic Analysis of Naturally Fractured Reservoirs*, Texas, USA: Gulf Professional Publishing, 2001.
- [51] Q. LEI, J.-P. LATHAM and C.-F. TSANG, "The use of discrete fracture networks for modelling coupled geomechanical and hydrological behaviour of fractured rocks," *Computers and Geotechniques*, vol. 85, pp. 151-176, 2017.
- [52] E. BARROS , "Chapter 4. Naturally fractured carbonate reservoirs.," in *Geomechanics, Fluid Dynamics and Well Testing, Applied to Naturally Fractured Carbonate Reservoirs*, Springer, 2018, pp. 77-89.

- [53] S. AGAR and G. HAMPSON , "Fundamental controls on flow in carbonates: an introduction," *Petroleum Geoscience*, vol. 20, no. 1, 2014.
- [54] M. ABBASI and P. ROSTAMI, "Generalized analytical solution for gravity drainage phenomena in finite matrix block with arbitrary time dependent inlet boundary condition and variable matrix block size," *Journal of Petroleum Science and Engineering*, vol. 167, pp. 227-240, 2018.
- [55] G. V. CHILLINGARIAN , S. J. MAZZULLO and H. H. RIEKE, "Chapter 10. Fluid Flow through Carbonate Rock Systems," in *Carbonate Reservoir Characterization: A Geologic-Engineering Analysis*, Elsevier, 1996.
- [56] N. AYAWEI, A. NEWTON and D. WANSAKI, "Modelling and Interpretation of Adsorption Isotherms," *Hindawi Journal of Chemistry*, no. Department of Chemical Sciences, Niger Delta University, September 2017.
- [57] R. HELMIG, "Mathematical Modelling," in *Multiphase Flow and Transport Processes in the Subsurface*, Springer, 1997, pp. 114-131.
- [58] W. FREEDEN and Z. NASHED, "Efficient Modeling of Flow and Transport in Porous Media Using Multiphysics and Multiscale Approaches," in *HANDBOOK OF GEOMATHEMATICS*, Orlando, FL, Springer, 2010, pp. 417-452.
- [59] Y. CENGEL and M. BOLES, "Chapter 4 first law of thermodynamics," in *Thermodynamics: An Engineering Approach*, Edición: 7th (2011), McGraw-Hill.
- [60] R. H. BROOKS and A. T. COREY, "Properties of Porous Media Affecting Fluid Flow," *Journal of the Irrigation and Drainage Division*, vol. 92, no. 2, pp. 61-90, 1966.
- [61] Z. CHEN, G. HUAN and Y. MA, "Computational methods for multiphase flows in porous media," *Computational Science & Engineering*, 2006.
- [62] A. GRAUE, "Wettability Effects on Oil-Recovery Mechanisms in Fractured Reservoirs," *SPE Reservoir Evaluation & Engineering*, vol. 4, no. 6, pp. 455-466, 2013.
- [63] S. SHADDEL, "Low Salinity Water Flooding: Evaluating the Effect of Salinity on Oil and Water Relative Permeability, Wettability and Oil Recovery," *Special Topics and Reviews in Porous Media*, vol. 05, no. 02, 2014.

- [64] P. GHOSAL and A. GUPTA, "Development of a generalized adsorption isotherm model at solid-liquid interface: A novel approach," *Journal of Molecular Liquids*, vol. 24, pp. 21-24, 2017.
- [65] A. KUMAR, "Chapter 9. Surface chemistry," in *Numerical Chemistry*, New Delhi, McGraw Hill Education, 2012, pp. 267-294.
- [66] J. SMITH and W. COBB, Waterflooding, Midwest Office of the Petroleum Technology Transfer, 1997.
- [67] J. C. SECCOMBE, A. LAGER, K. J. WEBB and G. JERAULD, "Improving Waterflood Recovery: LoSaltTM EOR Field Evaluation," *SPE Journal*, 2008.
- [68] S. E. JØRGENSEN, "Chapter 6. Adsorption," in *Industrial Waste Water Management*, Copenhagen, Denmark, ELSEVIER, 1979, pp. 61-80.
- [69] T. D. VAN GOLF-RACHT, "Naturally Fractured Reservoirs," in *Fundamentals of Fractured Reservoir Engineering*, ELSEVIER, 1982.
- [70] C. QIAO , R. JOHNS and L. LI, "Modeling Low-Salinity Waterflooding in Chalk and Limestone Reservoirs," *Energy Fuels*, vol. 30, pp. 884-895, 2016.
- [71] T. AUSTAD, S. STRAND , M. MALLAND and T. PUNTERVOLD, "Seawater in Chalk: An EOR and Compaction Fluid," *SPE Journal*, p. 648, 2008.
- [72] P. ZHANG and T. AUSTAD, "Wettability and oil recovery from carbonates: Effects of temperature and potential determining ions," *Colloids and Surfaces A: Physicochemical and Engineering Aspects*, vol. 279, no. 1-3, pp. 179-187, 2006.
- [73] J. J. SHENG, "Transport of Chemicals and Fractional Flow Curve Analysis," in *Modern Chemical Enhanced Oil Recovery: Theory and Practice*, Elsevier, 2010.
- [74] G. A. POPE, "The Application of Fractional Flow Theory to Enhanced Oil Recovery," *Society of Petroleum Engineers Journal*, vol. 20, no. 03, 1980.
- [75] S. H. PRASSETYO, M. GUTIERREZ and N. BARTON, "Nonlinear shear behavior of rock joints using a linearized implementation of the Barton–Bandis model," *Journal of Rock Mechanics and Geotechnical Engineering*, vol. 9, no. 4, pp. 671-682, 2017.

